Time-lapse airborne EM for monitoring the evolution of a saltwater aquifer the Bookpurnong case study

Signora, Alessandro; Munday, Tim; Vonk, Martin Arie; Fiandaca, Gianluca

DOI
10.1093/gji/ggaf414

Publication date
2025

Document Version
Final published version

Published in
Geophysical Journal International

Geophysical Journal International

Geophys. J. Int. (2025) **244,** 1–22
Advance Access publication 2025 October 29
Research Paper

https://doi.org/10.1093/gji/ggaf414

Time-lapse airborne EM for monitoring the evolution of a saltwater aquifer—the Bookpurnong case study

Alessandro Signora [1], Tim Munday,[2] Martin Arie Vonk[3,4] and Gianluca Fiandaca [1]

[1] *The EEM Team for Hydro & eXploration, Department of Earth Sciences A. Desio, University of Milan, Via Mangiagalli 34, 20133, Milan, Italy, alessandro.signora@unimi.it*
[2] *The Commonwealth Scientific and Industrial Research Organization, CSIRO Mineral Resources, 26 Dick Perry Ave., 6151, Kensington, Perth, Western Australia*
[3] *Department of Water Management, Faculty of Civil Engineering and Geosciences, Delft University of Technology, Stevinweg 1, 2628, Delft, The Netherlands*
[4] *Artesia B. V., Korte Weistraat, 2871 BP, Schoonhoven, The Netherlands*

Accepted 2025 October 14. Received 2025 October 3; in original form 2025 February 26

SUMMARY

A novel time-lapse modelling scheme for airborne electromagnetic (AEM) monitoring data sets is presented, using data from multiple surveys applied to study the hydrorelated evolution of the Bookpurnong floodplain in South Australia. Additionally, it introduces a new wide-ranging approach for this type of study, incorporating new processing, validation and interpretation tools.

Time-lapse studies are widespread in the literature but are not commonly applied to model electromagnetic (EM) data, particularly AEM data. This is linked to the challenges of performing overlapping data acquisition with inductive systems. The key features of the present time-lapse scheme include the definition of independent forward and model meshes, essential for considering discrepancies in the location of soundings which arise in multitemporal AEM data acquisition. Moreover, the incorporation of system flight height in the inversion revealed important for achieving satisfactory data fitting and limiting artifact propagation in the time-lapse models.

A novel processing workflow for AEM multitemporal data sets is also presented. This has proven important for effectively processing the multitemporal data sets, which presents new challenges in identifying noise coupling arising from the use of different systems across vintages of data, possible variations in acquisition settings operated by different field crews, and changes in subsurface resistivity in the survey area. Results generated from the time-lapse modelling are evaluated with an independent hydrogeological validation (IHV), designed to support the geophysical models validation and interpretation by providing a first-step hydrogeological evaluation.

At Bookpurnong, along a sector of the Murray River floodplain, multitemporal AEM surveys were collected in 2015, 2022 and 2024, to study natural and engineered changes in the groundwater system over time. The time-lapse models show significantly smaller variations compared to those determined with individually modelled survey data sets, while delineating sharply bounded changes in resistivity across the floodplain. This highlights the effectiveness of the new time-lapse scheme in minimizing inversion variations typically encountered with independently modelled results affected by larger equivalence issues.

Here, AEM models are first compared with resistivity borehole measurements, revealing a close match between the two methodologies and spatial variations in resistivity consistent with a meandering river across the floodplain. These variations are further validated and interpreted using the IHV approach, which revealed a direct correlation between the hydrological stress of the Murray River and the response of shallow aquifers. Additionally, time-lapse geophysical models, combined with a hydrostratigraphic analysis, allow for a direct correlation between shallow and deep hydrogeological responses.

We believe that the time-lapse methodology described here can be widely applied to multitemporal studies using AEM data sets, enabling the study of a broad range of natural processes with great accuracy and at the basin scale.

Key words: Electrical properties; Electromagnetic theory; Time-series analysis.

1 INTRODUCTION

Airborne electromagnetic (AEM) surveys have seen growing application in recent years for environmental and hydrogeological studies (see, for example, Viezzoli *et al.* 2009; Knight *et al.* 2018; Goebel *et al.* 2019; Chandra *et al.* 2019, 2021; Dumont *et al.* 2021; Minsley *et al.* 2021) demonstrating their ability to effectively characterize subsurface electrical properties across large areas with everimproving precision. An overview on AEM for environmental, geotechnical and hydrogeological applications is provided by Auken *et al.* (2017). AEM systems enable the collection of data over hundreds of line kilometres in a single day, with measurements typically taken every few tens of metres and reaching depths of several hundred metres. Furthermore, improvements in system accuracy and data repeatability, both crucial in multitemporal geophysical analysis, now permit the consistent detection of the subsurface with sufficient precision to capture subtle changes over time. This is particularly important in hydrogeophysical studies at the basin scale, where imaging hydrogeologically related processes with appropriate resolution is crucial.

Geophysical temporal studies have evolved from traditional comparison of separate inversions to time-lapse frameworks: They aim to emphasize data-driven changes in the models while minimizing variations caused by noise, inversion artifacts and limiting equivalences issues. Various time-lapse modelling procedures have been proposed in the literature, often employing specialized noise cancellation techniques. Examples include the ratio inversion (Daily *et al.* 1992), the cascaded inversion (Oldenborger *et al.* 2007; Miller *et al.* 2008) and the difference inversion (LaBrecque & Yang 2001).More recently, time-lapse approaches have been developed to integrate two or more time steps into a simultaneous inversion, incorporating all data sets within a unified framework (e.g. Kim *et al.* 2009; Hayley *et al.* 2011; Karaoulis *et al.* 2011a,b). Despite the considerable time since the introduction of time-lapse techniques, examples detailing the application of AEM in such studies remains scarce in the literature (e.g. Beamish & Mattsson 2003; Hauser *et al.* 2025).

Several practical factors have limited the application of AEM for monitoring compared to, for instance, multitemporal galvanic studies. These include the relatively high cost of AEM surveys, the challenges in precisely matching EM sounding locations between repeated surveys, changes in flight heights as well as the use of different EM systems and variations in their configuration and field operation.

Additionally, the limited availability of modelling codes capable of handling AEM time-lapse data has likely hindered the broader adoption of such approaches. The constrained development of such tools likely stems from the inherent challenges of time-lapse AEM inversion, which demands forward algorithms that properly model the different AEM system characteristics so that subtle changes in the subsurface are detectable. While major variations can often be captured without time-lapse approaches, detecting small, yet meaningful, differences requires that only data-driven changes are reflected in the results. Ultimately, the sensitivity to such subtle variations should be limited by the resolution of the AEM system itself and not by the modelling accuracy.

To address the issue of limited tools for time-lapse inversion, we propose a novel, simultaneous, time-lapse inversion scheme tailored for AEM applications that can handle multitemporal and multisystem acquisitions presenting discrepancies in EM sounding locations and flight heights. Together with this inversion scheme, we present a dedicated processing workflow for AEM monitoring data, aiming for consistent and efficient multitemporal data set processing.

These inversion and processing schemes are applied to an AEM monitoring data set composed of three surveys (approximately 20 km^2 in extent each), conducted with different SkyTEM time domain EM systems (Sorensen & Auken 2004) over the Bookpurnong floodplain in South Australia. The goal of this study was to understand water quality exchanges over time between the highly saline aquifers and the Murray River as it meanders through its floodplain. We reached this goal, not only by analysing the geophysical results themselves, but also through an Independent Hydrogeological Validation (IHV). The IHV is a novel operational tool intended to bridge geophysics and hydrogeology and, in this study, to validate the time-lapse models in addition to the more traditional approach using borehole resistivity measurements. Within the IHV, the Murray River streamflow and water quality trends are analysed, providing insights into their impact on the underlying hydrogeological system.

In the following, the time-lapse modelling strategy for the geophysical data is presented first, followed by its application to the Bookpurnong study. Before presenting and validating the temporal evolution of this site, its hydrostratigraphic description is provided.

2 MODELLING STRATEGY

2.1 Geophysical modelling

The time-lapse inversion of AEM data in this work is carried out within the EEMverter (Fiandaca *et al.* 2024), in a simultaneous process in which all different data sets are inverted at once, with a data space d defined as

$$d = \left[d_1, \cdots, d_{N_{\mathrm{TL}}}\right] \tag{1}$$

in which d_i represents the i-th data sets and N_{TL} represents the number of different time-lapse data sets.

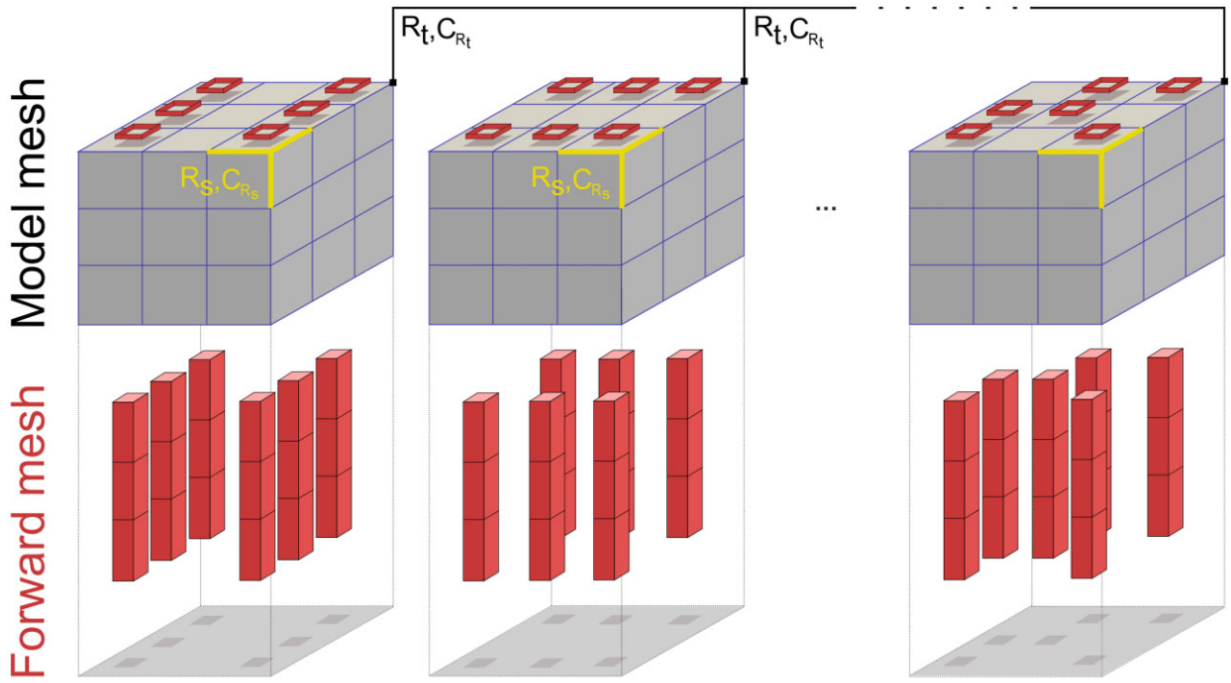

Figure 1. Model and forward mesh architecture for time-lapse modelling in EEMverter, where identical model meshes (3-D grey meshes) are defined and linked to their corresponding irregularly distributed forward meshes (1-D red meshes) through interpolation. The sketch highlights also the two types of mesh regularization applied: vertical/horizontal intramodel constraints (yellow lines and labels) and temporal model constraints (black lines and labels).

For each data set d_i, a corresponding model vector M_i is defined, with the whole inversion model space defined as:

$$M = \left[M_1, \cdots, M_{N_{\mathrm{TL}}}\right] \tag{2}$$

Each model M_i contains two types of inversion parameters, the resistivity and the flight height: the resistivity is defined on a regular mesh, while the flight height is defined sounding-by-sounding. The inclusion of the flight height in the inversion process can be of great help for obtaining acceptable misfit and/or models in the time-lapse inversion, particularly in low-resistivity environments. In such environments, a small error in the height estimation can lead to shallow time-lapse artifacts and/or in worsening data fitting, with typical airborne height measurements accuracy ranging between 0.3 and 1 metre, depending for instance on the system pitch angle.

The regular mesh for the definition of resistivity is then linked to a forward mesh for forward/Jacobian computations, following the approach presented for instance in Christensen *et al.* (2017) for 1-D EM computations and in Zhang *et al.* (2021), Engebretsen *et al.* (2022) and Xiao *et al.* (2022b) for 3-D EM computations. The link between inversion meshes (hereafter named model meshes) and forward meshes is obtained through an interpolation: the inversion parameters M (i.e. resistivity in this study) are defined in the model meshes and then interpolated onto the forward meshes (with m indicating the interpolated parameters), for the computation of forward response and Jacobian. The interpolation is carried out with a simple linear operator as:

$$m_i = A_i \cdot M_i \tag{3}$$

where the index i represents the time-lapse index of the data sequence and the matrix A contains the interpolation weights, computed with a first-order inverse distance approach. Fig. 1 reports a sketch of model and forward meshes architecture just described for a time-lapse inversion with $N_{\mathrm{TL}} = 3$.

The decoupling of model and forward meshes allows for a straightforward implementation of time-lapse inversion for surveys in which the data acquisition has non-coincident sounding positions, as it always happens in AEM applications: The model meshes for all temporal acquisitions can coincide in space, while the forward meshes follow the sounding positions.

The inversion is carried out with an iterative re-weighted least-squares (IRLS) approach (Farquharson & Oldenburg 1998) that minimizes the objective function Q defined as

$$Q = \sqrt{\frac{(d - f(M))^T \cdot C_{\mathrm{d}}^{-1} \cdot (d - f(M)) + M^{\mathrm{T}} \cdot R_{\mathrm{s}}^{\mathrm{T}} \cdot C_{R_{\mathrm{s}}}^{-1} \cdot R_{\mathrm{s}} \cdot M + M^{\mathrm{T}} \cdot R_{\mathrm{t}}^{\mathrm{T}} \cdot W^T \cdot C_{R_{\mathrm{t}}}^{-1} \cdot W \cdot R_{\mathrm{t}} \cdot M}{N_{\mathrm{d}} + N_{R_{\mathrm{s}}} + N_{R_{\mathrm{t}}}}}, \tag{4}$$

where C_{d}, $C_{R_{\mathrm{s}}}$ and $C_{R_{\mathrm{t}}}$ are the data and roughness covariance matrices (the subscripts s and t indicate space and time in the roughness regularization), the matrices R_{s} and R_{t} determine the constrained parameters and W represents a re-weighting of the least-squares matrices for applying norms different from the L2.

The roughness matrices R_s and R_t are defined as:

$$R_s = \begin{bmatrix} R_{s_1} & \cdots & 0 \\ \vdots & \ddots & \vdots \\ 0 & \cdots & R_{s_{N_{TL}}} \end{bmatrix} \tag{5}$$

$$R_t = \begin{bmatrix} R_{t_{1+}} & R_{t_{2-}} & \cdots & 0 & 0 \\ \vdots & \vdots & \vdots & \vdots & \vdots \\ 0 & 0 & \cdots & R_{t_{N_{TL}-1+}} & R_{t_{N_{TL}-}} \end{bmatrix} \tag{6}$$

In eq. (5) the space-roughness matrix, indicated as R_s, is a block-sparce matrix where each R_{s_i} matrix contains the vertical and horizontal constraints within model M_i.

In eq. (6) the space-roughness matrix R_t is composed by blocks that link each M_i to the next-in-time model M_{i+1} through $R_{t_{i+}}$ and $R_{t_{i+1-}}$ pairs (with $+1$ and -1 indicating the model differentiation).

Thanks to the decoupling between model and forward meshes and the spatial correspondence of the resistivity model meshes, the constraint strength defined in C_{R_t} is uniform, regardless of the varying positions of the AEM soundings in the different data sets. The time-roughness is defined using the asymmetric generalized minimum support (AGMS) norm defined in Fiandaca *et al.* (2015), which minimizes the volumetric differences among constrained models. For tuning the AGMS settings, the guidelines suggested in Fiandaca *et al.* (2015) were followed in both the synthetic and field data inversions presented in this study. In particular:

(i) The p_1 and p_2 settings, which controls the transition sharpness of the AGMS norm, were set to the prescribed values for time-lapse inversions, namely $p_1 = 1.35$ and $p_2 = 2.0$, that is, values that give the weaker dependence of the focusing on the settings σ and α;

(ii) The setting σ, which control the focusing sharpness, was set to $\sigma = 5$ per cent ($\sigma = 0.05$ as relative variation), to fully penalize in the focusing resistivity variations above 15 per cent, that is, the typical variation values seen in the independent inversions of the field data;

(iii) The setting α, which controls the relative weight of data and time-lapse measures in the objective function and affects the size of the time-lapse changes, was set to $\alpha = 1.0$, allowing for time-lapse variations over 10–30 per cent of the model; with this value, as shown in the next paragraph, the time-lapse inversion of the data gives data misfit fully comparable to the independent inversion, ensuring that the relative weight between data and time-lapse measures is well balanced.

For completeness, the values of smoothness constraints contained in the C_{R_s} matrix were set in all the inversions of this study as $\sigma_{\text{vertical}} = 2.0$ and $\sigma_{\text{horizontal}} = 0.3$ (values expressed as relative variation between constrained parameters).

The n + 1th model update of the IRLS inversion procedure is computed as:

$$M_{(n+1)} = M_{(n)} + \left[G_{(n)}^{T} \cdot C_d^{-1} \cdot G_{(n)} + R_s^{T} \cdot C_{R_s}^{-1} \cdot R_s + R_t^{T} \cdot W'^{T}_{(n)} \cdot C_{R_t}^{-1} \cdot W'_{(n)} \cdot R_t + \lambda I\right]^{-1}$$
$$\cdot \left[G_{(n)}^{T} \cdot C_d^{-1} \cdot \left(d - f\left(M_{(n)}\right)\right) + R_s^{T} \cdot C_{R_s}^{-1} \cdot R_s \cdot M + R_t^{T} \cdot W'^{T}_{(n)} \cdot C_{R_t}^{-1} \cdot W'_{(n)} \cdot R_t \cdot M\right] \tag{7}$$

Where $G_{(n)}$ represents the jacobian of the nth iteration, which is a block-sparse matrix defined as

$$G = \begin{bmatrix} G_{M_1} & \cdots & 0 \\ \vdots & \ddots & \vdots \\ 0 & \cdots & G_{M_{N_{TL}}} \end{bmatrix} \tag{8}$$

in which G_{M_i} represents the jacobian of the i-th model and data sets. For computing the Jacobian of the parameters defined on the model meshes G_{M_i}, the Jacobian computed in the forward meshes is propagated through the chain-rule of differentiation as:

$$G_{M_i} = G_{m_i} \cdot {A_i}^{T} \tag{9}$$

Finally, the depth of investigation (DOI) in the inversion is carried out following Fiandaca *et al.* (2015b).

2.2.1 Synthetic example

The synthetic example in Fig. 2 further highlights the importance of these time-lapse constrains. In this instance, the same type of AEM data later used in the field study is tested on a 100 m long synthetic model representative of the expected subsurface electrical properties at the real site. Specifically, SkyTEM data, with a 10-m spacing between each EM sounding (red dots at the bottom of each model in Fig. 2), are used to generate the forward responses over models that mimic the growth of a high resistivity anomaly (50 Ω·m) over a low-resistivity half-space (1 Ω·m). In Fig. 2, time-lapse results are displayed as ratios obtained dividing the first model by the subsequent ones. The black-box shape shown across the models represents the true high-resistivity anomaly evolution. The EM data includes gate times ranging approximately from 6E-06 to 12E-03 s. The modelling, as described in the previous section, is carried out using a 1-D EM forward response and decoupled forward and model meshes, to ultimately compare the results obtained using independent and time-lapse frameworks. Both approaches use identical intramodel discretization and regularization to ensure that differences are solely due to the enforcement of AGMS temporal constraints in the time-lapse inversion.

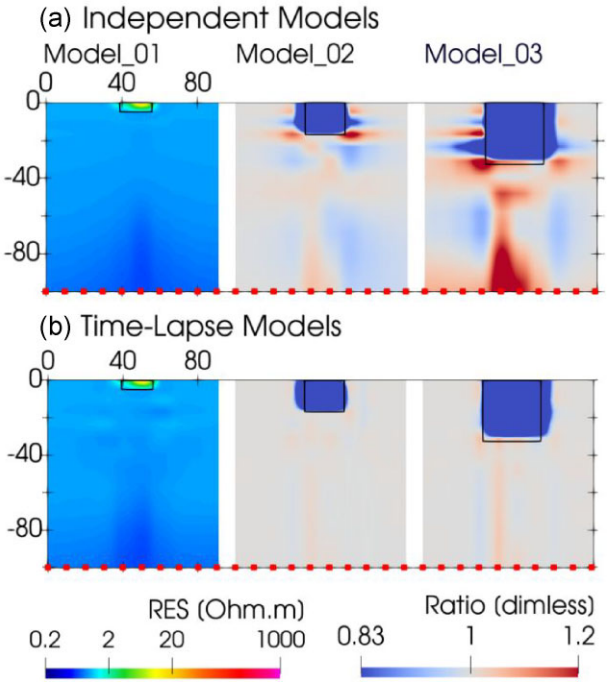

Figure 2. Synthetic test comparing independent and time-lapse schemes for inverting AEM temporal series. (a) Independent inversion models. (b) Time-lapse inversion models. From left to right in both (a) and (b), the true models simulate the growth of a high-resistivity anomaly with its true shape delineated by the overlaying black line. The models are shown over their DOI and the EM sounding positions are indicated at the bottom of each model (red dots).

In this noise-free example, the independent (Fig. 2a) and time-lapse (Fig. 2b) inversions exhibit significantly different models, while having an equivalent misfit value (approximately 0.3 in all cases). As expected, the time-lapse inversion yields more compact results due to the suppression of equivalence-driven artifacts thanks to the temporal regularization.

In the example of Fig. 2, the data was noise-free to highlight the characteristics of the time-lapse inversion and to reduce potential noise-related bias in the comparison. However, when repeating the same inversion with added noise—3 per cent gate uncertainty plus a time-dependent noise decreasing as $t^{-\frac{1}{2}}$ with level equal to 1 $\frac{nV}{m^2}$ at 1 ms—the models obtained with the time-lapse framework remained very similar. In contrast, the independent models further localize artifacts due to the noise effects. In both cases, the data fitting was equivalent, with misfit values close to 1. The noise-added example is not shown here for brevity, but the performance of the time-lapse framework in suppressing non-data-driven differences under realistic noise conditions will be extensively presented in the field application sections.

3 THE BOOKPURNONG CASE STUDY

The case study presented in this work is located on a stretch of land of approximately 20 km^2 referred to as the Bookpurnong floodplain, which forms part of the River Murray floodplain, in South Australia. In this part of the Murray Basin, the river, groundwater system and agricultural areas are heavily managed to cope with the natural high-salinity (as defined for instance in Van Engelen *et al.* 2018) of the shallow unconfined aquifers (see Section 3.1.1 for details).

The river has multiple weirs and locks where water levels are controlled. The river-aquifer interaction naturally forces saline water exchange towards the river, challenging the floodplain freshwater recharge. This directly threatens the survival of floodplain vegetation that depends on freshwater and complicates the use of groundwater for agricultural activities. River discharge and flood events are the primary source of freshwater recharge on the floodplain, but its natural hydrological balance is heavily influenced by the anthropogenic activities on and adjacent to the floodplain.

Numerous studies have focused on the Bookpurnong area using geophysical methods (Berens *et al.* 2004; Munday *et al.* 2005; Hatch *et al.* 2010; Viezzoli *et al.* 2009; Munday & Soerensen 2018), supporting hydrogeological investigations. The following sections present the time-lapse modelling of a series of AEM surveys repeatedly acquired over the Bookpurnong floodplain in 2015, 2022 and 2024, specifically aimed at describing spatial variations in the thickness, lateral extent and evolution of the freshwater (or low salinity) lens at a high resolution.

The freshwater exchange between the river and underlying/adjacent aquifers is the primary source of variations along the floodplain. In fact, water levels have been reported as able to exceed those of the river (as noted in Yan *et al.* 2005) and to average in depth few metres below the surface: Large-scale variations of water table are then assumed to be negligible in the AEM monitoring results, also considering that the surveys were conducted at similar times of year (see Fig. 13).

Both qualitative and quantitative analyses will be provided, with the spatiotemporal interpretation supported by geophysical validation through resistivity borehole measurements and through the Independent Hydrogeological Validation, offering an additional layer of integration between geophysics and hydrogeology.

3.1 Hydrogeological setting

3.1.1 Hydrostratigraphy

The Bookpurnong area lies within the Renmark Trough, a transitional zone where sedimentary sequences can reach thicknesses up to 500 m. These Cainozoic sediments form a closed groundwater basin, with the Murray River serving as the only surface connection to the Southern Ocean through its mouth. This hydrostratigraphical setting led to naturally high salinity in the aquifers, as rainfall, surface water and ground water accumulated within the basin over the past half a million years, combined with limited recharge capacity. For a comprehensive description, we refer to Brown (1989). The main regional lateral flow in the Bookpurnong area is from east to west, with floodplain water table located a few metres below the surface. As a result, highly saline groundwater discharges into the River Murray, where salt concentration can be 2–3 orders of magnitude lower than in the floodplain (see next bullet points and Fig. 13e). The site topography is characterized by highland and floodplain areas. The highlands have elevations ranging from approximately 30–50 m.a.s.l., while the River Murray has carved a floodplain valley with ground elevations between 9 and 18 m.a.s.l (Fig. 5a).

An overview of the geological units is sketched in Fig. 3 and listed below, including the maximum thickness and the salinity range of each formation, where available, as reported in Yan *et al.* (2005), which provides a more comprehensive description:

Woorinen Formation (Unsaturated): quaternary unconsolidated red-brown silty sand and clay (aeolian dune)
Blanchetown Clay (Unsaturated): quaternary lacustrine unit, locally silty/sandy. Found regionally within the unsaturated zone.
Loxton sands (Unconfined to semiconfined aquifer): highly heterogeneous coarse-grained sands transitioning into less permeable fine sands toward the base of the succession. These sands grade into low-permeability silty clay as they approach the Loxton Clay Formation (Max. Thickness: 38 m; Water Salinity: 2–64 g L^{-1}; Water Conductivity: 3–90 mS cm^{-1}).
Coonambigdal Formation (Aquitard): clay layer across the floodplain, consisting of clay and silt from episodic flooding (Max. Thickness: 11 m).
Loxton Clay and Bookpurnong Beds (Aquitard): poorly consolidated plastic silts and shelly clays (Max. Thickness: 25 m).
Monoman Formation (Unconfined to semiconfined aquifer): clean, fine-to-coarse fluvial sands, deposited as point bar sands (Max. Thickness: 25 m; Water Salinity: 13–46 g L^{-1}; Water Conductivity: 19–66 mS cm^{-1})
Pata Formation (Unconfined to semiconfined aquifer): poorly consolidated limestone with friable sand layers (Max. Thickness: 15 m; Water Salinity: 8–32 g L^{-1}; Water Conductivity: 11–46 mS cm^{-1})
Winnambool Formation (Aquitard): grey to pale green calcareous marl and silty clay (Max. Thickness: 7 m)
Glenforslan Formation (Semiconfined aquifer): grey sandy limestone, similar to Pata Formation (Max. Thickness: from 16–30 m; Water Salinity: 3–27 g L^{-1}; Water Conductivity: 4–39 mS cm^{-1}).
Finniss Formation (Aquitard): grey to dark grey clay with thin sand layers and hard bands (Max. Thickness: 14 m).
Mannum Formation (Confined aquifer): Well-compacted and cemented grey limestone. Upwards leakage reported from the underlying Renmark Group aquifer (Max. Thickness: 101 m; Water Salinity: 2–25 g L^{-1}; Water Conductivity: 3–36 mS cm^{-1}).

Yan *et al.* (2011) details the main horizontal flows within the hydrostratigraphic units but reports also vertical flows between different aquifers due to incomplete isolation of the aquitards. These upwards flows enable the interaction between the Murray Group (Pata, Winnambool and Glenforslan Formations in Fig. 3) and the water table aquifer (Monoman Formation), particularly in areas where the lower Loxton Clay and Bookpurnong Beds have been eroded. Yan *et al.* (2011) also report significant salinity variations with depth. At the same time, the river is considered to impact the ground water quality, with short-term fluctuations affecting the shallower Monoman Formation, while the Loxton Sands and the Murray Group respond to longer term trends.

Based on the hydrostratigraphy described above, the resistivity distribution on the floodplain is expected to be characterized by relatively high-resistivity anomalies (>10 Ω·m), corresponding to freshwater inputs from the Murray River, superimposed on a predominantly low-resistivity background (<2 Ω·m) representative of the high-salinity aquifers and clayey aquitards. Intermediate resistivity values are also expected in fresh–salt water transition zones. In terms of temporal changes, increases in resistivity values across the floodplain will likely be indicative of freshwater migration on the floodplain, whereas decreases in resistivity are expected to indicate salinization dynamics. Additionally, given the reported vertical connectivity between aquifers and the variability of salinity with depth, also vertical resistivity changes, due to upwards or downwards water flows, may be observed. Resistivity in the highlands is expected to be relatively high, comparable to river fresh water values or higher. River-induced variations are not expected there, rather saline aquifer recharge may occur through agriculture drainage and irrigation of orchards grown in these areas which adjoin the floodplain.

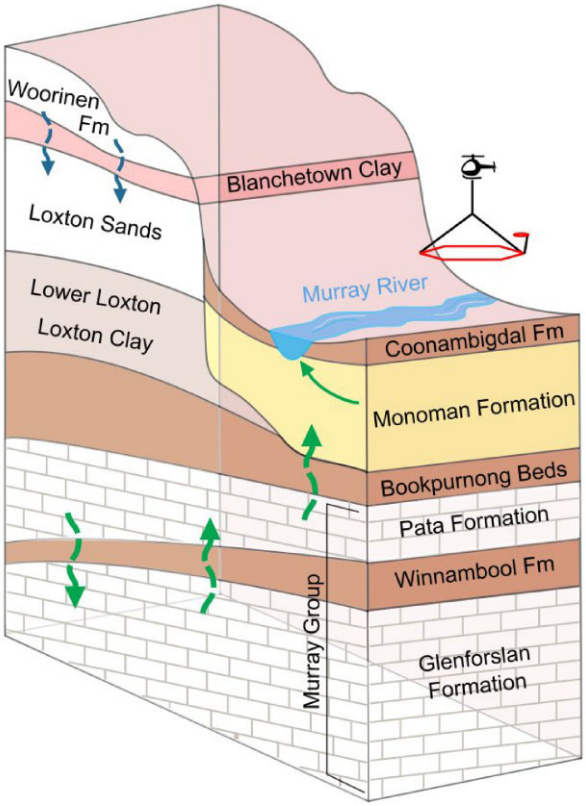

Figure 3. Sketch depicting the hydrostratigraphic setting at the Bookpurnong site. The diagram is not to scale.

3.1.2 Water management of the area

The River Murray is managed by several locks and weirs, with lock (and weir) 4 inside the case study area. At the Locks, measurements of the river water level, discharge and electrical conductivity are provided (SA Water 2018). At the Bookpurnong floodplain site, recharge of the shallow aquifer is heavily influenced by the irrigation drainage in highland areas, significantly affecting salinity distribution in the floodplain. Agricultural freshwater drainage to the underlying saline aquifer has increased its hydraulic gradient encouraging saline groundwater discharge into the river, which in turn prompted the construction of the Saltwater Interception Scheme (SIS) to mitigate its impact. In the Bookpurnong area, the SIS system, part of a larger-scale implementation across the region, is situated near the southeast meander of the river. Positioned at the foot of the highland bank, where it joins the floodplain, the SIS extracts salt water and diverts it into a disposal basin located further east. In lowering the hydraulic gradient form the highland to the river, it favours fresh water ingress from the river into its banks and the adjoining saline floodplain sediments.

3.2 Geophysical survey and data processing

The geophysical data set gathered in the Bookpurnong area consists of a multitemporal airborne EM data set measured in 2015, 2022 and 2024 (Fig. 5a). Each survey overlaps the same flight lines, covering around 200 line kilometres, with 30 acquisition lines of ∼7 km each, spaced approximately 100 m. The temporal acquisitions are designed to ensure data comparability between closely located measurements. Tie-lines were also measured to assess data quality both at the time of acquisition and across different surveys. The May 2015 survey employs the SkyTEM^{304} system, which features a rigid transmitter (TX) with a 340.8 m^2 area and dual-moment energization with nominal peak currents of 9 A and 116 A featured by current turn-off ramp times of 3.5 and 50 μs, respectively (Fig. 4, red lines). It is worth underscoring that no data can be retained before the transmitter current is fully shut down. The respective TX OFF-times are 1.018 and 10 ms, with acquisition frequencies of 275 and 25 Hz, allowing the accurate retrieval of early and late times. The receiver (RX) is mounted in the so-called zero position, where the RX coil is positioned to minimize the primary field flux interference. The RX features a 105 m^2 area with a 210 kHz low-pass cut-off frequency filter for the Z component and a high-moment front gate time of 70 μs. In June 2022, the AEM survey employs a SkyTEM^{312} FAST system to overlap the same lines. The dual-moment measurement strategy remains, using a transmitter with an area of 342 m^2. The respective peak currents for the High Moment (HM) and Low Moment (LM) are 6 and 110 A, with repetition frequencies of 275 and 25 Hz, turn-off ramp times of 12 and 300 μs and OFF-times of 1.018 and 15.0 ms (Fig. 4, green lines). The 2022 system is expected to provide the lower shallow resolution compared to the other systems due to its slower LM current shut

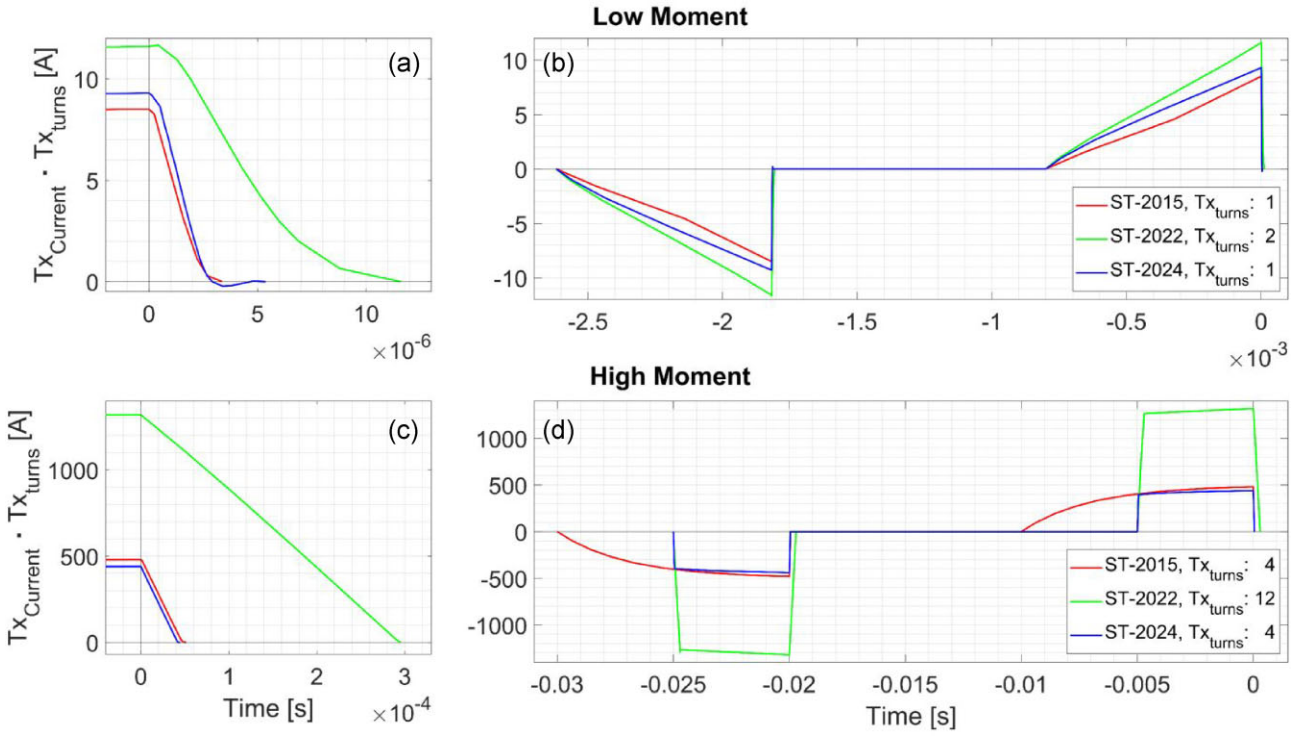

Figure 4. Energization characteristics of the SkyTEM systems used in the 2015 (red), 2022 (green) and 2024 (blue) Bookpurnong monitoring. The first row shows the low-moment energizations, highlighting the shut-down ramp (panel a) and a complete measuring cycle (panel b). The second row (panel c and d) details the high-moment energizations.

down (Fig. 4a). The receiver coil, placed in the zero-position, is featured with a 206.8 kHz low-pass cut-off frequency for the *Z* component and a front gate time of 370 μs for the HM. In March 2024, the survey was conducted using the SkyTEM[304] system, which differs from the system used in 2015 for the TX area of 342 m^2, the HM current of 110 A, current turn-off ramp times of 5.5 μs for the LM and 42 μs for the HM, HM OFF time of 15 ms (Fig. 4, blue lines) and an RX area of 325 m^2 with a cut-off frequency of 203 kHz for the *Z* component.

The processing of AEM data occurs at different stages, possibly leading to terminology ambiguity depending on the context. Hereinafter, by pre-processing we refer to the raw data manipulation performed by the contractor after acquisition and before delivery to the client (e.g. stacking, filtering, etc.). By data processing, we refer to the culling of delivered data based on their noise content and proximity to coupling structures.

In this work, the data processing is carried out following the recommendations presented in Viezzoli *et al.* (2013), with particular attention given to identify small power lines that cross the Bookpurnong area, as well as other major noise sources such as roads and infrastructures. The data processing is performed with a novel 'simultaneous' approach, made possible by the flexible handling capabilities of the EEMStudio (Sullivan *et al.* 2024). This approach is designed for processing temporal AEM series with overlapping flight lines, ensuring first that the same coupling-affected areas were removed across all data sets by defining the most conservative data-cleaning distance from the structure and applying it consistently. Furthermore, this workflow was necessary to assess noise content that appeared to vary temporally across different data sets. In fact, during the multitemporal data processing, noise disturbances near specific infrastructure were evident in one data set but less pronounced in others.

An example of this is shown in Fig. 6, where a small power line disturbance is clearly visible in the SkyTEM 2015 (Fig. 6c) and 2024 (Fig. 6e) data sets, while SkyTEM 2022 data set (Fig. 6d) shows almost noise-free transients for the same location. Fig. 6 provides just one example of the many similar cases identified during the Bookpurnong floodplain data processing, almost always linked to small power lines (Fig. 6b) that cross the area. In most cases, we could rule out the possibility that these issues arose from newly constructed infrastructure, since the disturbances were absent in one of the later acquisitions even though the presence of such structures was already confirmed by historical maps (Google Earth LLC., LAT:-34.35°, LONG: 140.57°—WGS84). Moreover, in the instance of Fig. 6, such noise-content differences were not ascribed to variations in systems ground height, as the systems were flown at approximately 40 m above ground in all three surveys over this section. The coupling behaviour was also not attributed to the lateral distance from the power line. In fact, the most disturbed transients are from the 2024 data set (blue dots), which are the farthest from the power line pylon, while the least coupled data are from the 2022 data set (green dots), which are closest to the pylon location.

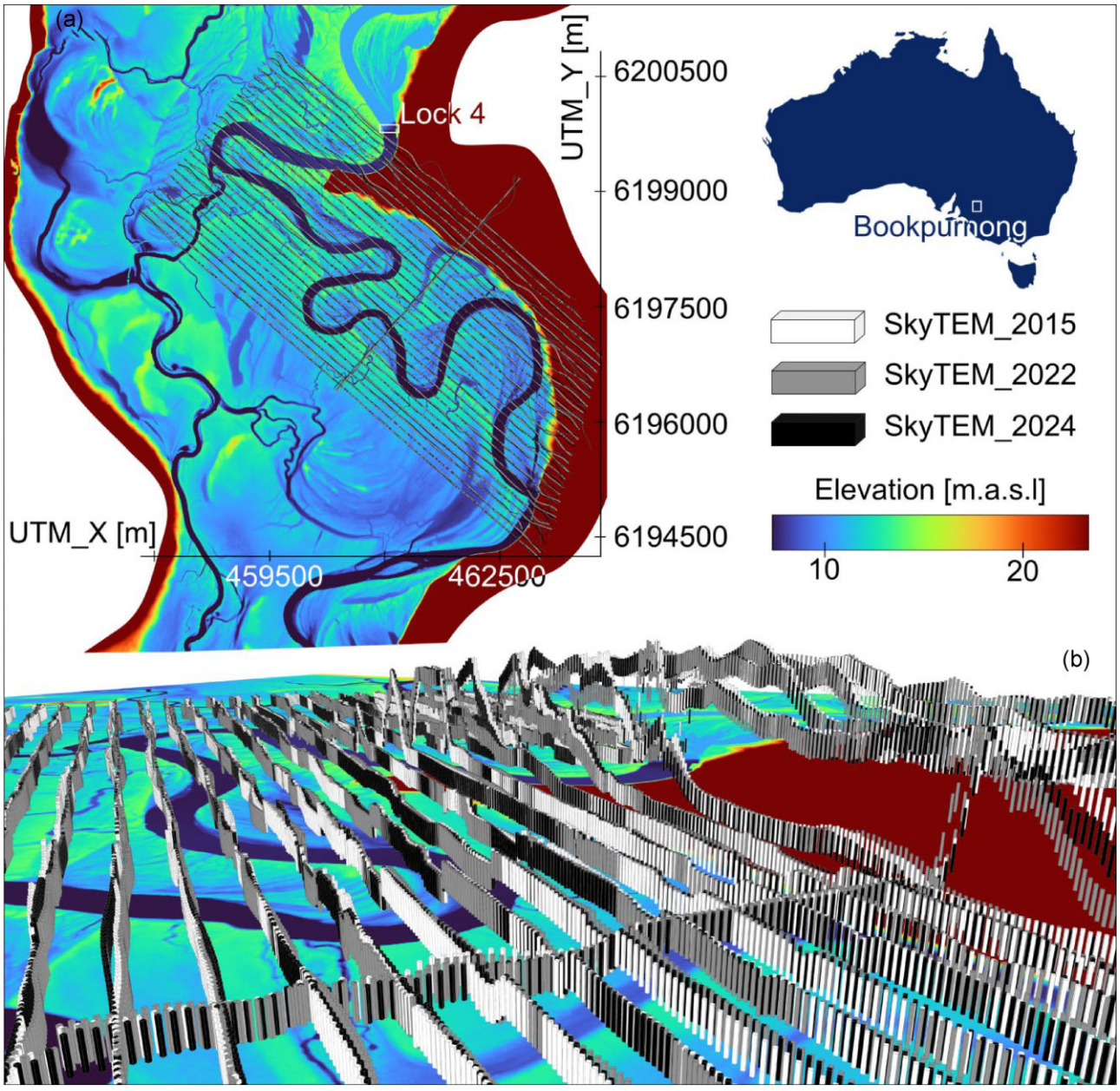

Figure 5. (a) LiDAR derived elevation map of the Bookpurnong area overlined by the AEM survey lines (2015, 2022, 2024) included in the time-lapse study. Lock 4 on the Murray River, a source of hydrogeological data for the next analysis, is also shown. (b) Close-up view of the AEM soundings distributed across the floodplain, emphasizing the varying spatial positions of data points on temporal-overlapped survey lines.

Questions remain open regarding the reasons behind these different effects observed in the delivered data. Such variations may arise from differences in the pre-processing performed by the data provider, as well as from variation in the mutual induction between the AEM transmitter and receiver coils and the power line due to the relative orientation more than the relative distance.

Nonetheless, this could have led to model artifacts if the data sets were processed separately as it would have been difficult to identify the small power lines by analysing just one data set at the time, as in the case of SkyTEM 2022 of Fig. 6. The 'simultaneous' approach aimed for the most conservative processing by allowing to cull out all data (both the LM and HM) that presented coupling in any of the multitemporal datasets and/or were measured near a coupling structure.

3.3 Data modelling and geophysical validation

The data modelling follows the workflow outlined in Section 2.1, employing a 1-D EM forward response with accuracy within 1 per cent when compared to AarhusInv (Auken et al. 2015). Viezzoli *et al.* (2010) demonstrated that this 1-D modelling approach is an adequate approximation

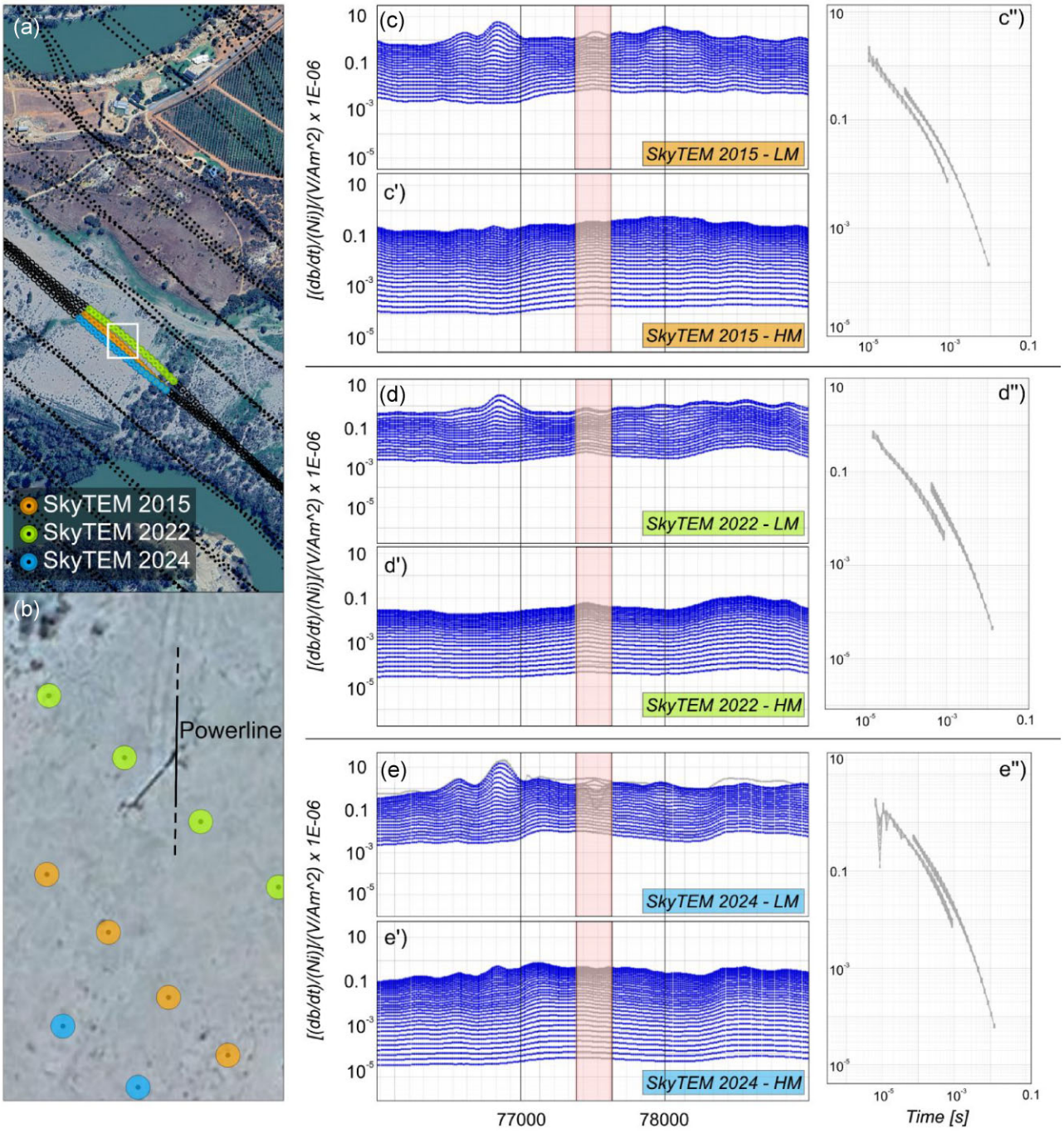

Figure 6. Different effects of the power line on the Bookpurnong 2015, 2022 and 2024 data sets. (a) Zoomed-out map. The coloured dots indicate the EM soundings removed, highlighted by the red boxes in the panels on the right. The white square indicates the location of the power line. (b) Zoomed-in view of the power line on the floodplain, whose north–south direction is indicated by the black line. (c, c′, c′′) SkyTEM 2015 data for Low and High moments, with EM transients removed from the selection highlighted by the light red box. (d, d′, d′′) Similar to the previous description, but for the SkyTEM 2022 data. (e, e′, e′′) Similar to the previous description, but for the SkyTEM 2024 data.

for depicting the hydrogeological features of this site. After the data processing, a total of 13868, 15734 and 14741 EM soundings were included in a first independent inversion round of the 2015, 2022 and 2024 data sets, respectively. The same data are subsequently unified within the time-lapse inversion framework. The purpose of running the independent inversions first is to establish a reference for tuning the time-lapse inversion and enable comparison between the two approaches on a real data application, allowing to move beyond the synthetic example (Section 2.2.1).

Independent and time-lapse inversions were configured with some shared characteristics. Both follow a multicycle process (Fiandaca *et al.* 2024), starting with a preliminary cycle designed to run a single-layer inversion to set better starting values than homogeneous or

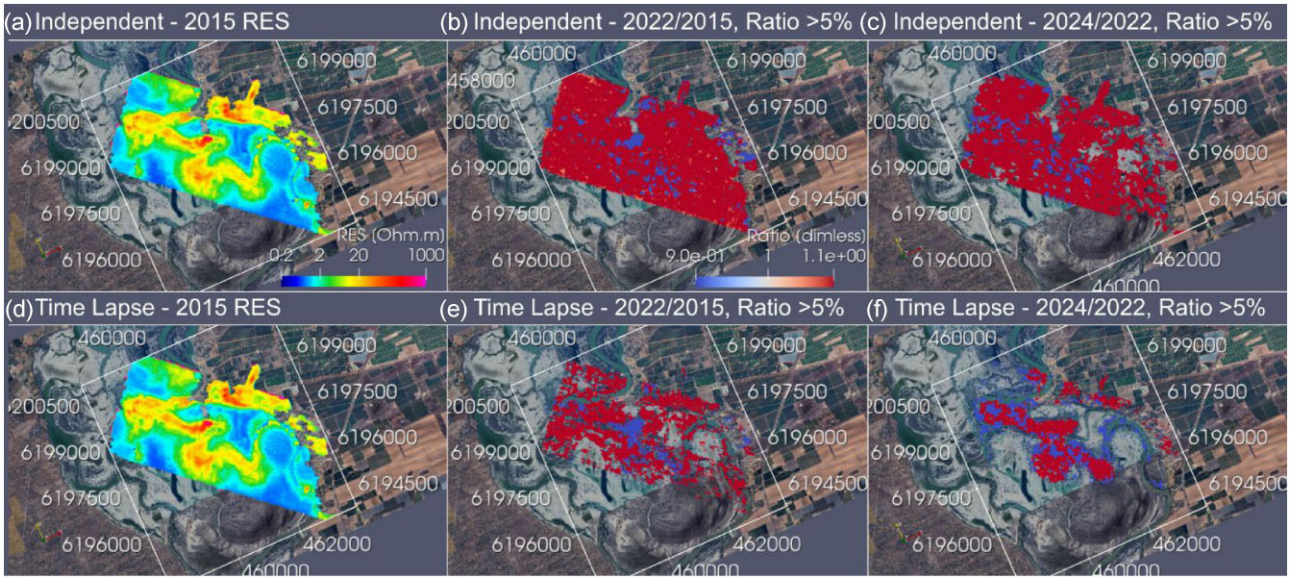

Figure 7. Real-case comparison of independent and time-lapse inversions performed on the Bookpurnong data sets. (a) 2015 resistivity model obtained through independent inversion. (b) Ratio of 2022 to 2015 independent resistivity models. (c) Ratio of 2024 to 2022 independent resistivity models. (d) 2015 resistivity model obtained through time-lapse inversion. (e) Ratio of 2022 to 2015 time-lapse resistivity models. (f) Ratio of 2024 to 2022 time-lapse resistivity models. All ratio model shows differences greater than ±5 per cent.

gradient. This step preceded the subsequent multilayered cycle, where the model discretization consisted of 21 layers logarithmically spaced from 5 to 500 m. This discretization was found to strike a good balance between system resolution, investigation targets and the computational cost of the time-lapse inversion.

The regularization remained consistent between the independent and time-lapse models and employed an L2 norm and vertical and horizontal constraints which allow model variations of up to 200 and 30 per cent, respectively. The strength of the spatial and temporal constraints has been kept constant to avoid introducing bias in time-lapse differences due to inhomogeneous regularization. Data uncertainties were incorporated through the inverse of the covariance matrix included in eq. (4), accounting for them in the model updates. Regarding the model space parametrization, the AEM system flight height was included as an inversion parameter for both the independent and time-lapse inversions. This addition was important for achieving satisfactory misfit in both approaches as the system flight height has a significant impact on the computation of AEM responses, especially when operating in conductive environments where the sensitivity on this parameter is stronger.

As presented in Section 2.1, the time-lapse approach defines the forward and model meshes independently to account for the varying locations of EM soundings across different data sets. Time-lapse constraints are enforced between model meshes, using AGMS-type constraints with settings: $\alpha = 1$, $\sigma = 0.05$, $p_1 = 1.35$ and $p_2 = 2.00$ (see Section 2.1 for the explanation of the setting choice).

Fig. 7 reports the models obtained for the different years from both the independent and time-lapse inversion approaches. In the upper row, the independent models are presented: the 2015 model is displayed in terms of resistivity values (Fig. 7a), followed by the ratio between the 2022 and 2015 resistivity models (Fig. 7b), and the ratio between the 2024 and 2022 resistivity models (Fig. 7c). In the lower row, the corresponding time-lapse models (Figs 7d–f) are shown. Here and in the following, all resistivity models are cropped over their DOI and when ratio models are computed, they are limited to the most conservative DOI among the two models involved in the ratio.

In the ratio panels of Fig. 7, only variations greater than ±5 per cent are displayed to isolate significant changes. Consistently with the results from the synthetic experiment (Fig. 2), the time-lapse modelling reveals significantly more compact/conservative estimates of change compared to the independent inversion results.

3.3.1 Misfit analysis

Regarding the misfit comparison between independent and time-lapse inversions, Table 1 presents the misfit values obtained for each model from both approaches, which are almost identical.

A uniform noise model was applied to the modelling of all three data sets, with the data gate standard deviations set to a minimum of 3 per cent, summed with the standard deviation measured during the stacking procedure. For instance, Fig. 8(b) shows the gate-by-gate standard deviation for all EM soundings acquired (prior to our processing) by SkyTEM in 2024. Thanks to the high signal-to-noise characteristics of the site, only the last few gates of the high moment display a slight increase in standard deviation.

The spatial distribution of the misfit is also alike between independent and time-lapse models. This ensures that the values of AGMS setting used in this study are conservative, i.e. favour (or do not hinder) data fit in contrast to focusing of the time-lapse anomalies (in

Table 1. Data misfit values for the independent and time-lapse inversions of the Bookpurnong AEM surveys conducted in 2015, 2022 and 2024.

Data Misfit	SkyTEM^{304}–2015	SkyTEM^{312}FAST–2022	SkyTEM^{304}–2024
Independent inversions	1.22	0.78	0.80
Time-Lapse inversion	1.22	0.78	0.79

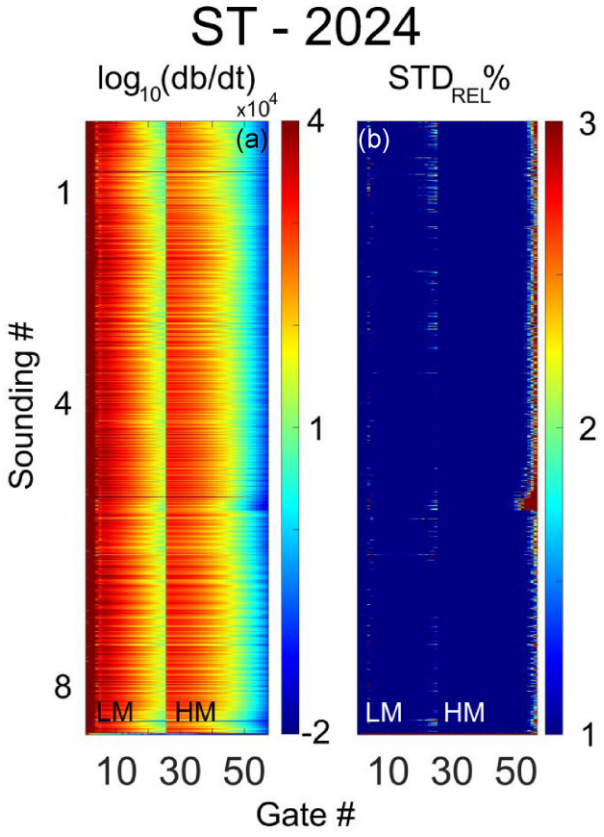

Figure 8. Data (panel a) and relative standard deviation (panel b) for all gates of the low and high moment of the EM soundings acquired during the SkyTEM 2024 survey. The reported data are prior to data processing.

particular for the setting α, which controls the relative weight of data and time-lapse measures in the objective function and affects the size of the time-lapse changes).

Fig. 9 further illustrates the misfit distribution and the specific fitting of the decay curves. Figs 9(a), (d), and (g) display the 'Gate-by-Gate' spatial distribution of the misfit, plotted according to the position of each EM sounding in the area for the 2015, 2022 and 2024 surveys, respectively. In this visualization, the misfit for each gate, defined as $\phi_{\mathrm{GATE},\,i} = \frac{|d_{\mathrm{GATE}_{\mathrm{obs}},\,i} - d_{\mathrm{GATE}_{fwr},\,i}|}{\sigma_i}$, is plotted vertically, where the vertical position of each gate is given by $z_{\mathrm{GATE},i} = \frac{i}{N} \cdot z_{\max}$. Here, i represent the index of the i-th gate, N is the total number of gates, and $z_{\max}$ is the maximum depth of the model. Since SkyTEM is a dual moment system, the first gate number for the High Moment correspond to $i_{\mathrm{First,\ HM}} = N_{\mathrm{LM}} + 1$, where N_{LM} is the total number of gates for the Low Moment data. This representation enables the identification of any spatial correlation in the misfit, and aids in visualizing systematic issues in the fitting of specific gates. This helps to pinpoint areas where certain gates might exhibit poor fits, revealing potential inconsistencies or issues in the data also across the temporal data sets. Examples of this can be observed by examining the 2015 and 2022 misfit distributions across gates and space. In the 2015 data set (Fig. 9a), systematic issues are evident in the early Low Moment gates, as well as a poorly fitted band corresponding to the early High Moment gates. Additionally, the 2022 misfit distribution exhibits an interesting behaviour (Fig. 9d), where the misfit for the first 2–3 low-moment gates increase sharply in the southern half of the survey compared to the same gate times in the northern part. These systematic misfits appear equivalent also in the independent inversions. There is no additional information available to explain these misfit patterns, though in 2022 case it could be due to an interruption between survey flights resulting in system changes. The 2024 survey appears to be uniformly well-fitted throughout (Fig. 9g).

To the right of each Gate-by-Gate misfit plot, the data (blue lines) and fit (black lines) are shown for a survey line (Figs 9b, e, h) and for some individual transients extracted (Figs 9c, f, i). This visualization confirms the overall satisfactory fitting.

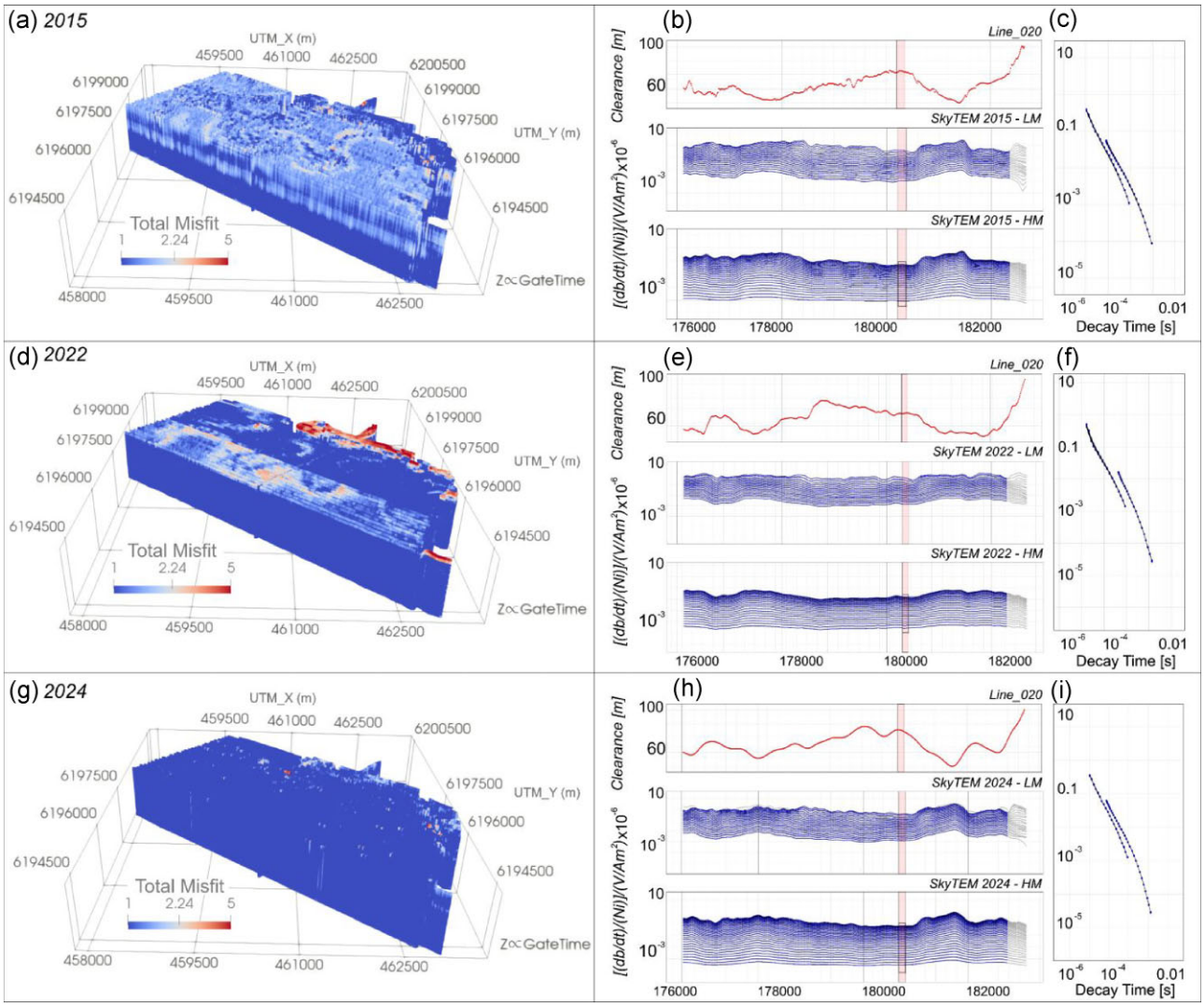

Figure 9. Spatial misfit analysis from the time-lapse inversion of the AEM series acquired over Bookpurnong. (a, d, g) Gate-by-gate spatial distribution of the misfit for the 2015, 2022 and 2024 data sets, respectively (*Z*-axis is proportional to gate time). (b, e, h) Comparison between data (blue line) and fit (black line) for the LM and HM components. The upper plots show system ground clearance/height. (c, f, i) Comparison between data (blue line) and fit (black line) for EM transients extracted from the area marked by a black box and red padding.

As it will appear when presenting the inversion models, the systematic change in misfit behaviour of the 2022 survey across the floodplain does not introduce any correlated structure in the time-lapse inversions. On the contrary, the higher systematic misfit observable in the 2015 inversion probably triggers a localized time-lapse difference at around −35 to −55 m of elevation, as further commented in Section 3.4.

3.3.2 Comparison with borehole logging

Before proceeding with the interpretation phase, the models are assessed by complementing the misfit analysis with borehole resistivity and geomorphological comparisons. This analysis focuses on the 2022 time-lapse model as, in June of that year, two borehole log-EM measurements have been collected near an AEM survey line and close to a secondary channel of the Murray River (Fig. 10). In Fig. 10(a), two AEM lines are extracted and the log-EM measurement locations highlighted. The sections are presented with a 10× vertical exaggeration, and the 3-D interpolated model is overlaid with light transparency. This visualization highlights first how the high-resistivity features consistently align with the river channel and banks, demonstrating strong coherence between the model and the primary geomorphological features. Fig. 10(b) allows the comparison between the closest AEM line to the log-EM borehole measurements, placed approximately 10 m apart from the flight line. The match between the borehole log-EM data and the time-lapse model is precise, demonstrating the capability of the AEM model to delineate the high-resistivity anomaly associated with the secondary channel of the Murray River. This is achieved despite the coarser vertical discretization compared to the log-EM sampling (∼10 cm spacing). The blue mesh at the end of the section displays a portion of the AEM model mesh, with vertical discretization equal to that used for the 1-D forward mesh. Figs 10(c) and (d) offer a more quantitative comparison, showing the 1-D log-EM measurements (RMK_406 and RMK_407) plotted alongside the five closest 1-D AEM models. This

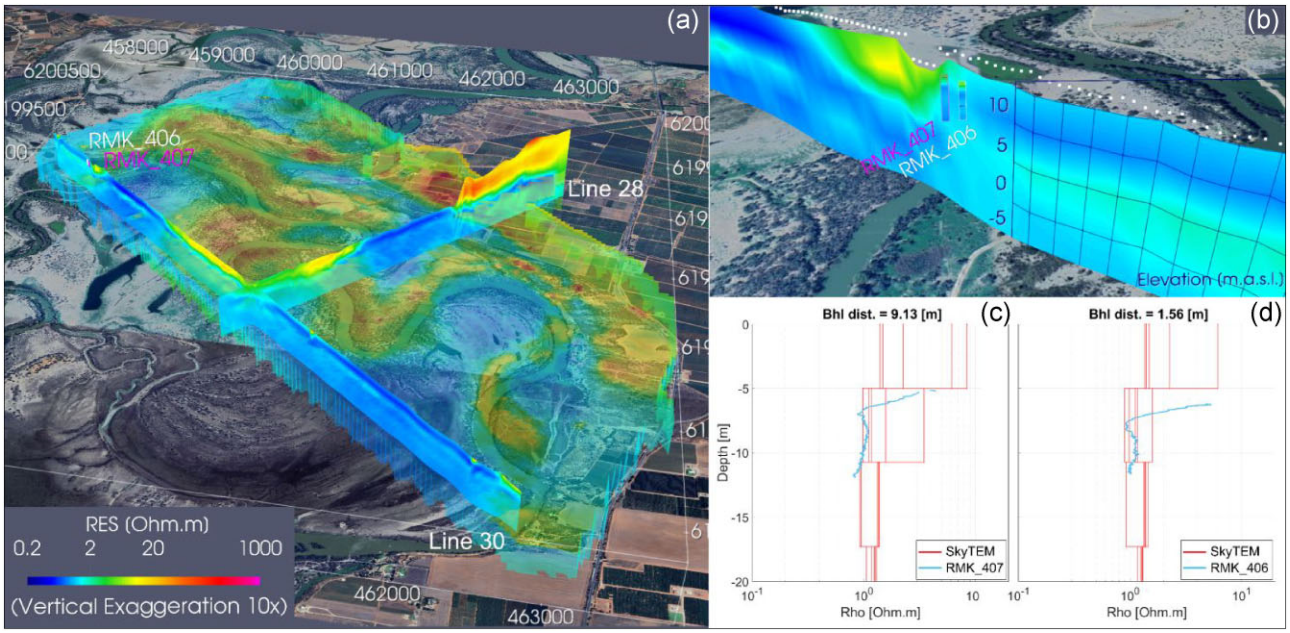

Figure 10. Comparison between the 2022 time-lapse AEM geophysical model and two log-EM measurements (RMK_406 and RMK_407), collected in June 2022. (a) 2-D sections for Line_28 and Line_30, showing the relative positions of the two log-EM measurements. (b) Detailed view of Line_30 close to the borehole locations. The blue grid on the right represents the model mesh. Each white dot along the section indicates the position of an EM sounding. (c, d) 1-D comparison between the RMK_407 and RMK_406 log-EM measurements and the five closest 1-D models extracted from the 2-D line. The vertical scale is expressed as depth from the surface.

last comparison further confirms the inversion ability to capture the transition from high-resistivity values near the river channel to lower resistivity at greater depths.

3.4 Site evolution analysis

The evolution of the Bookpurnong area in terms of electrical resistivity is first analysed by displaying the ratios between the time-lapse geophysical models at different depths. Fig. 11 presents depth slices at different elevations for the 2015 (panels a–h), 2022 (panels i–p) and 2024 (panels q–x) models. The 2015 model is used as the baseline and is reported in absolute resistivity values. For the 2022 and 2024 models, resistivity variations are presented as cell-by-cell ratios of the model mesh: the 2022 model is divided by the 2015 model, and the 2024 model by the 2022 model. This chronological analysis is meant to display the progressive temporal evolution of the site. In the ratio models, blue anomalies indicate a decrease in electrical resistivity compared to the previous time step, while red anomalies show an increase. The colorbar for the ratio models is displayed on a logarithmic scale where no-change areas appear in neutral white, while regions of increasing or decreasing resistivity intensify in colour, proportionally to the magnitude of temporal variation.

The ratio analysis shows that most of the investigated volumes present no significant variations (white zones), with bounded areas nearby to the river channel that present spatially coherent differences. These localized variations confirm the capability of the AEM time-lapse approach to handle data sets acquired with different systems and non-coincident flight lines. In turn this highlights the value of the AEM method on this type of monitoring.

The 2022 model displays an increase in resistivity in the shallow portions (Figs 11j and k) from to 2015, especially at the elevation corresponding to the river channel. Deeper down a significant resistivity reduction follows near the model bottom (Figs 11o and p). It is worth noting the presence of a high-resistivity anomaly, located between −35 and −55 m of depth, and clearly visible in the animation linked via the QR code of Fig. 11 (see also Signora, 2025a). This anomaly arises from the ratio between the 2022 and 2015 data sets, where the 2015 data exhibited a misfit issue in the early gates of the HM (see Fig. 9a). Therefore, we consider this resistivity feature to result from this issue and deem it unlikely to be real. It will not be further analysed, as it is outside the primary depth range of interest for the shallow river–aquifer interaction. However, should this depth range become of interest, a more detailed examination will be necessary. An alternative perspective on this uncertain high-resistivity band is presented in Fig. 12(e).

In 2024, the evolution is nearly opposite to the 2022, showing a widespread decrease in shallow layers resistivity (Figs 11r and s) and a strong resistivity increase below −70 m, peaking at the model bottom (Figs 11w and x). In this case, no resistivity anomalies are visible in the −35 to −55 m depth range, further suggesting data issues in the 2015 data set.

Notably, the time-lapse models reveal opposite evolution in resistivity values between the shallow and deeper deposits. Nevertheless, the deep variations (Figs 11p and x) among the years show a very similar spatial distribution, with well-defined boundaries corresponding to an

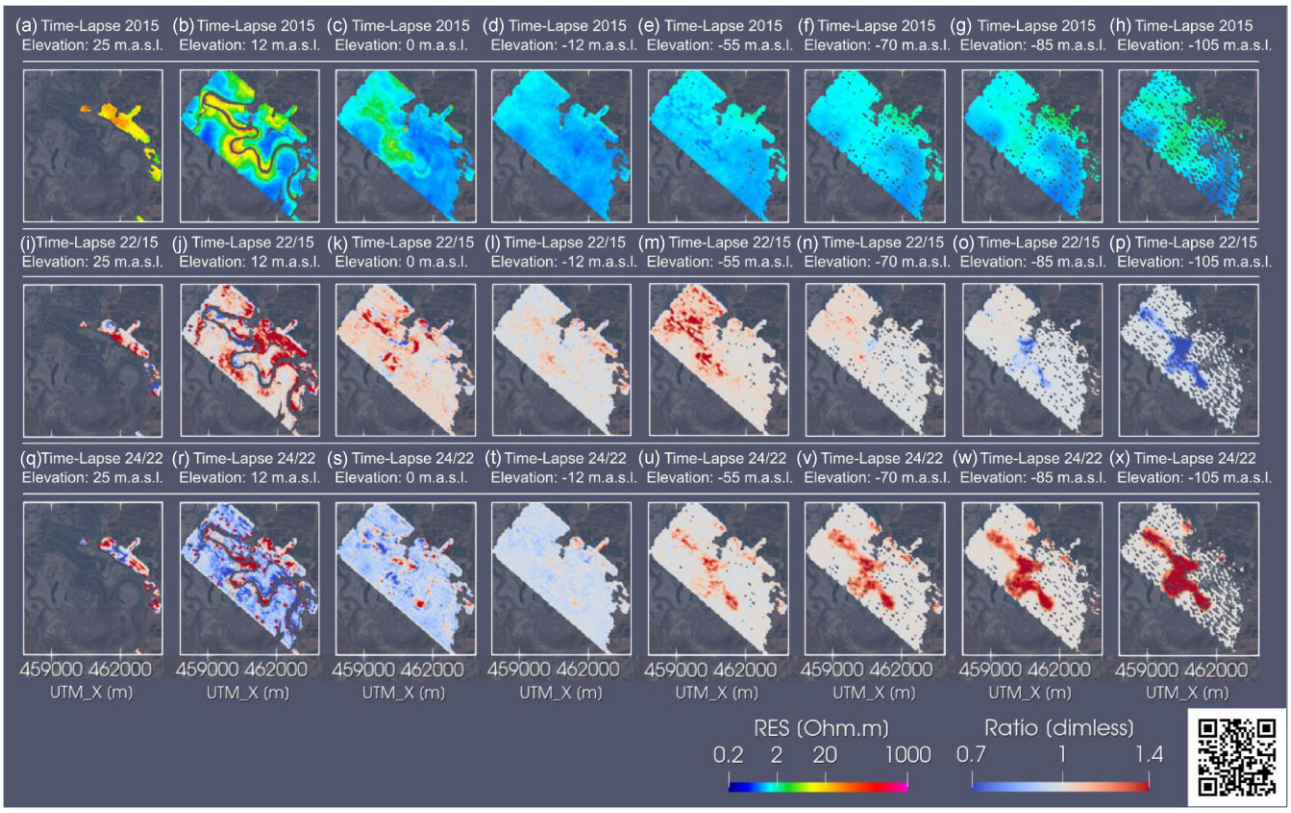

Figure 11. Depth slices from the time-lapse models obtained from the 2015, 2022 and 2024 AEM surveys. (a–i) Resistivity depth slices from the 2015 model. (j–p) Corresponding depth slices showing the cell-by-cell resistivity ratio between the 2022 and 2015 models. (q–x) Depth slices showing the ratio between the 2024 and 2022 models. In the ratio depth slices no-change areas appear in neutral white colour. Scan the QR code to access the depth slices animation.

area directly beneath the river channel. As these anomalies approach the lower DOI limit, a test was performed—confirming the modelling sensitivity to these structures (details and results are reported in Appendix A).

To further assess the model variations over the years, Fig. 12 presents vertical sections extracted to intersect multiple times the alternation between the river channel meanders and the floodplain. In Figs 12(a)–(c), the sections are displayed as resistivity values, while in Figs 12(e)–(f), they are shown as ratios between models, consistently with the approach used in Fig. 11. In Figs 12(a)–(c), the areas with compatible freshwater values, indicated by the high-resistivity anomalies, extend from the surface to a depth of approximately −20 m in elevation. The vertical axis marks the −10 m elevation level, which roughly corresponds to the depth of the river channel. The ratio sections (Figs 12e and f) confirm the trends observed in Fig. 11. In the 2022 model, there is an increase in resistivity in the shallow (from the surface down to −20 m.a.s.l.) and mid-depth sections (−35 to −55 m.a.s.l.), where the previously mentioned misfit issues occur. In contrast, the deeper model shows a decrease in resistivity. In 2024, a generalized decrease in resistivity is observed in the upper section, without significant changes at mid-depths, and an increase in resistivity at greater depths. For a more comprehensive evaluation, a video displaying sections across the entire floodplain is available via the QR codes provided in Fig. 12 (Signora, 2025c).

3.4.1 Independent hydrogeological validation of shallow-model evolution

The hydrostratigraphy of the Bookpurnong area consists of alternating aquifers and aquicludes (Fig. 3), with naturally occurring ground water characterized by high salinity. Salinity levels vary both horizontally within the same hydrogeological structure and vertically between different aquifers. The Murray River serves as the primary source of freshwater, sustaining the shallow aquifer (Yan *et al.* 2005). The observed variations in the time-lapse geophysical models are therefore likely associated with changes in groundwater quality, driven by freshwater infiltration from the Murray River into lateral deposits.

This hypothesis can be tested using an IHV, a novel approach based on the available time-series data from the Murray River and designed to bridge geophysics and hydrogeology. Specifically, time-series of the discharge, water level and salinity of the Murray River are analysed where the water level and salinity data are measured at different locks on the river and flows calculated using site-specific rating tables (SA Water 2018).

Fig. 13 presents geophysical depth slices just below the river channel elevation, displaying the resistivity distribution at 7 m.a.s.l. for the May 2015 model (Fig. 13a) alongside the ratio models for June 2022 and March 2024 (Figs 13b and c). Figs 13(d)–(f) presents the River

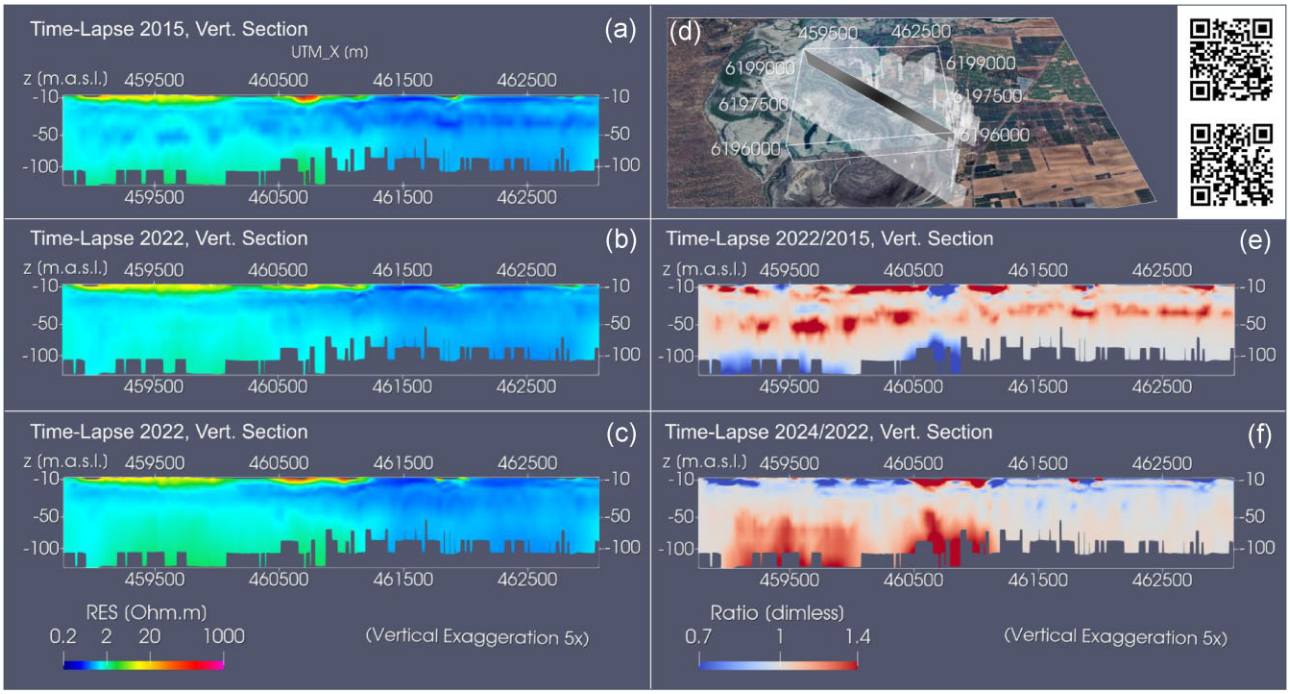

Figure 12. Vertical sections from the time-lapse models obtained from the 2015, 2022 and 2024 AEM surveys. (a–c) Resistivity vertical sections extracted at the location indicated in panel (d). (e) Vertical section showing the cell-by-cell ratio between the 2022 and 2015 models. (f) Vertical section showing the cell-by-cell ratio between the 2024 and 2022 models. Scan the QR code to access the vertical section animations (top and bottom QR codes for RES and ratio analysis, respectively).

Murray time-series for water level, salinity and discharge, respectively. The water level and salinity are extracted from Lock 4. The discharge is selected from Lock 7 since no discharge measurements were available at lock 4. The red lines overlying the discharge plot indicate the AEM survey dates.

The comparison of geophysical depth slices with time-series data starts on 2015 May 20 (Fig. 13a), when river discharge was relatively low (∼50 $m^3\ s^{-1}$). At this time, the AEM depth slice reveals high-resistivity values concentrated near the river channel, suggesting fresh water infiltration into lateral deposits and highlighting the influence of river discharge on the hydrogeological system. By June 2022, when the first ratio depth slice is available, river discharge had significantly increased to 300–550 $m^3\ s^{-1}$, with water levels approximately 2.5 m higher. This higher streamflow likely enhanced freshwater infiltration, as evidenced by a widespread increase in resistivity values (red areas in Fig. 13b). This suggests an intensified exchange and dispersion of fresh water into the lateral deposits, driven by elevated river discharge. In May 2024, discharge levels had decreased to ∼100 $m^3\ s^{-1}$, similar to those of 2015, while electrical conductivity (EC) had risen to ∼400 $\mu S\ cm^{-1}$, twice as high as in 2015 and 2022. This decreased streamflow with increased water EC coincides with a pronounced reduction in electrical resistivity in the geophysical slice (Fig. 13c, blue areas), further indicating the dynamic interaction between river and infiltration of water into the surrounding deposits.

Although the discharge values in 2015 and 2024 are similar, the total amount of fresh water infiltration is influenced not only by the streamflow at a given time but also by historical streamflow and water quality. To illustrate this, Fig. 14 presents the resistivity ratio between the 2015 and 2024 models. Compared to the ratios shown in Fig. 13, the variations in magnitude are less pronounced, and the resistivity changes exhibit a patchier distribution. This figure confirms that the freshwater distribution in 2024 differs from that in 2015, despite the comparable streamflow rates. These observations support the hypothesis that, under similar streamflow conditions, the actual water balance is influenced by prior river discharge events. In the case of 2024, this includes the high-discharge levels in 2023 and, notably, a major flood in December 2022. The large-scale flooding event likely contributed to the observed spatial variability and patchy resistivity patterns, highlighting the long-term impact of past hydrological conditions on groundwater dynamics.

3.4.2 Deep-model evolution analysis

The IHV was intended to validate the changes observed in the shallow portion of the time-lapse geophysical models (elevation > −25 m.a.s.l.), supporting hydrogeological interpretations in the depth range of main focus for this study. This shallow section is particularly relevant for water management and the development of strategies to mitigate salinization.

The previous IHV does not extend to the deeper model analysis, whereas Fig. 11 shows changes occurring throughout the entire depth of the models, including significant variations down to the depth of investigation at −105 m. Fig. 15 offers a 3-D view to highlight the spatial relationships between the changes in the ratio models (Figs 15d and e) and the absolute resistivity values distribution (Figs 15a–c).

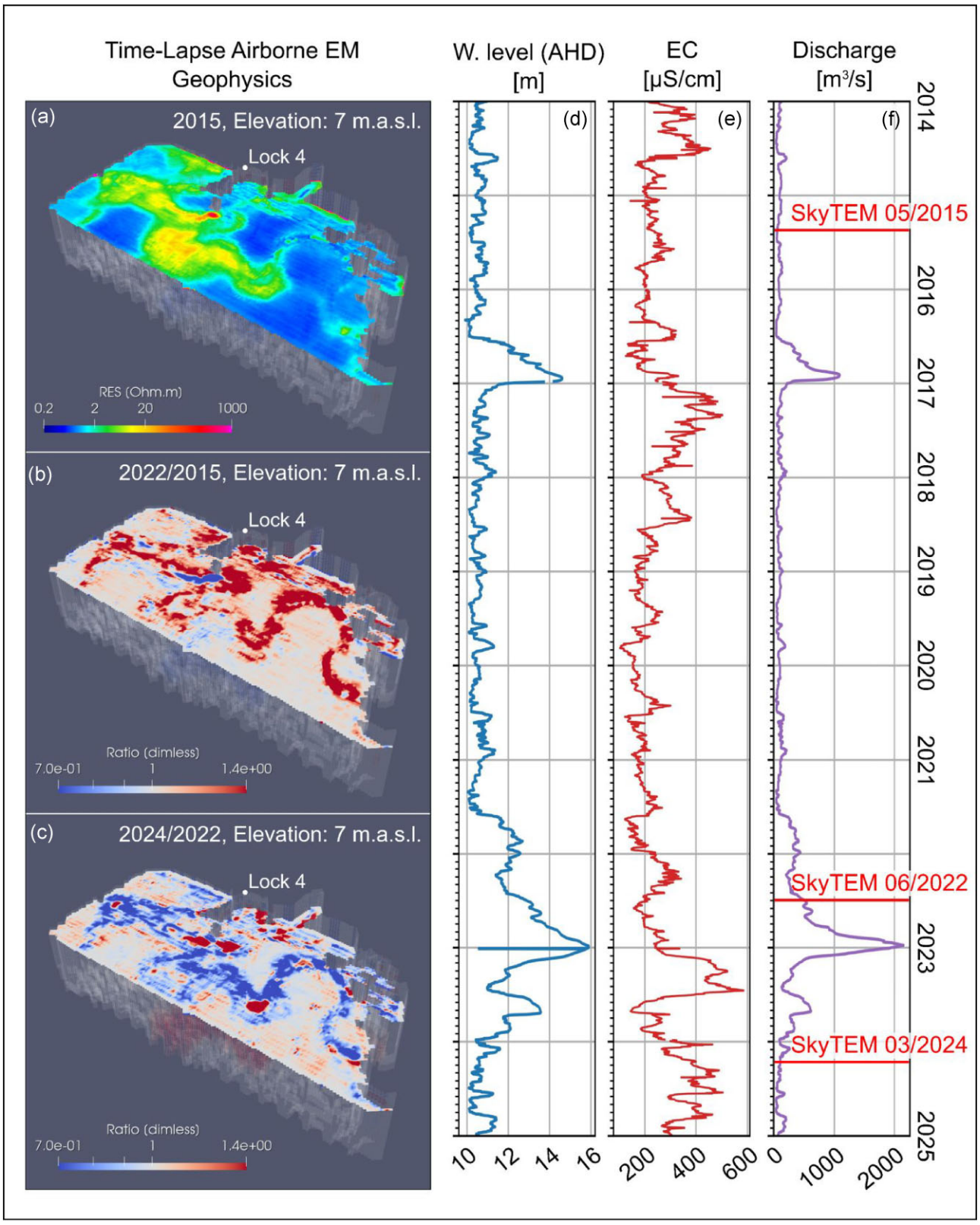

Figure 13. Comparison between the time-lapse AEM depth slices beneath the river channel elevation and the time-series hydrogeological indexes available for the site. (a) Resistivity model from the 2015 time-lapse inversion. (b) Ratio between the 2022 and 2015 time-lapse resistivity models. (c) Ratio between the 2024 and 2022 time-lapse resistivity models. (d) Water level series measured at lock 4 reported as meters AHD (Australian Height Datum). (e) Water salinity series measured at lock 4. (f) River Murray discharge as reported for lock 7 station.

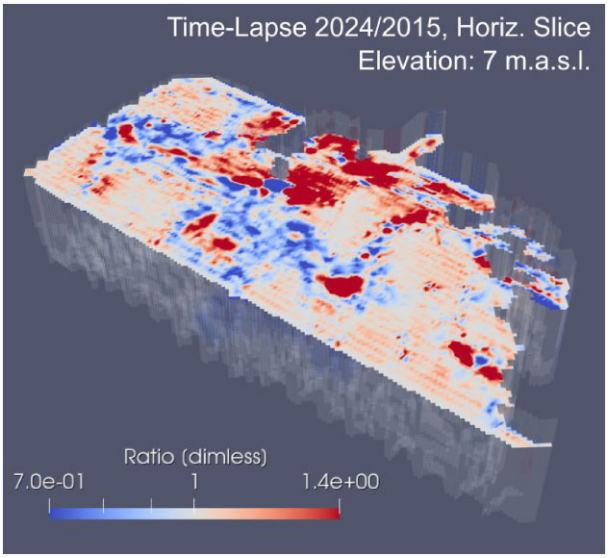

Figure 14. Ratio between the 2024 and 2015 time-lapse resistivity models

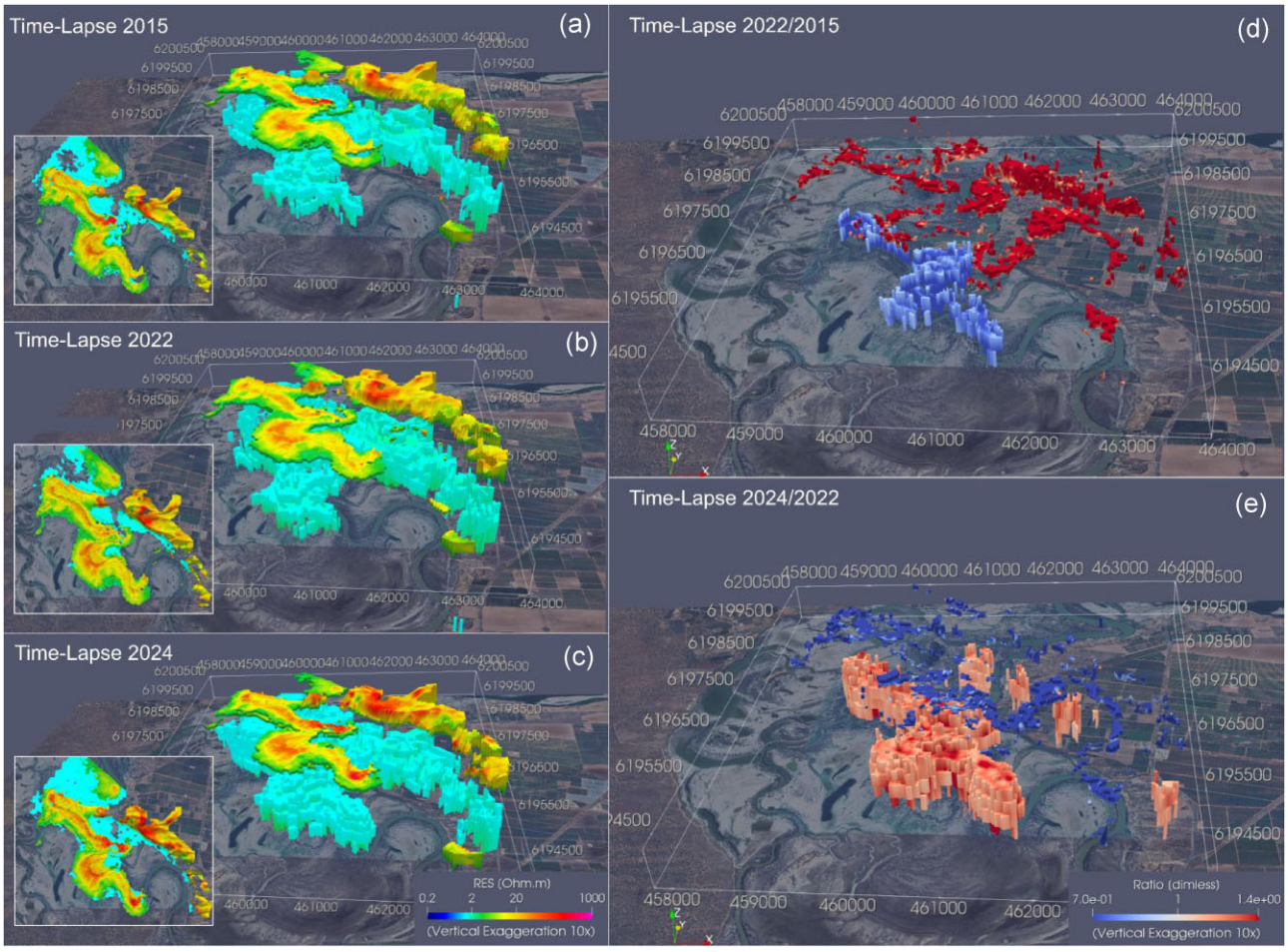

Figure 15. (a–c) Resistivity volumes extracted for the shallow part (Elevation > -25 m.a.s.l, Resistivity > 2 Ω·m) and the deep part (Elevation < -25 m.a.s.l, Resistivity > 1.5 Ω·m) from the 2015, 2022 and 2024 time-lapse models. The plan-view is shown in the bottom-left corner of each panel. (d, e) Volumes showing differences greater than ±8 per cent from the 2022/2015 and 2024/2022 ratio-models. Red colours indicate resistivity increases, and blue shows decreases.

Table 2. (a) Shallow and deep volumetric variations for the 2015, 2022 and 2024 resistivity models. For shallow volumes, extraction is based on resistivity values greater than 2 Ω·m. For deep volumes, the resistivity threshold is reduced to 1.5 Ω·m. Green-shaded cells highlight the year with the highest freshwater-like resistivity volumes in both shallow and deep model portions. (b) Volumetric variations exceeding ±8 per cent from the model ratios 2022/2015 and 2024/2022. Red shaded cells indicate the largest resistivity increases recorded across different years and at both shallow or deep depths.

	(a) RES			(b) RATIO	
	2015	2022	2024	2022/2015	2024/2022
	Volumes with $\rho > 2$ Ω·m [m^3]			Volumetric variations > 8 per cent [m^3]	
Shallow (>−25 m.a.s.l.)	3.68e07 ± 6 per cent	4.21e07 ± 4 per cent	3.59e07 ± 4 per cent	1.01e07 ± 9 per cent	3.06e06 ± 7 per cent
Deep (<−25 m.a.s.l.)	Volumes with $\rho > 1.5$ Ω·m [m^3]			Volumetric variations > 8 per cent [m^3]	
	8.8e07 ± 60 per cent	1.7e08 ± 70 per cent	1.98e08 ± 40 per cent	1.09e07 ± 9 per cent	1.43e + 08 ± 4 per cent

The resistivity volumes extracted in the latter frames aim to distinguish fresher water from the poorly resistive saline background (<1.5 Ω·m). In the shallow region (>−25 m.a.s.l.), near the river channel, resistivity values above 2 Ω·m are extracted, while in the deeper parts (<−25 m.a.s.l.), values greater than 1.5 Ω·m are displayed. Table 2 provides a quantitative breakdown of the high-resistivity volumes, separating shallow and deep regions. Confidence intervals for the extracted resistivity volumes were calculated as percentage variations by adjusting the lower and upper extraction limits by ±0.1 Ω·m. For the ratio models, the extraction limits were adjusted by ±1 per cent. Practically, for the shallow fresh water, the resistivity threshold was modified to 1.9 and 2.1 Ω·m, and the mean percentage variation was calculated relative to the volume extracted at the 2 Ω·m. The same procedure is applied to the deep fresh water volumes, this time varying the 1.5 Ω·m threshold. Consistently, for the ratio models, the 8 per cent threshold was varied to 7 and 9 per cent, and the mean percentage variation calculated. The volume analysis reveals that:

(i) The largest high-resistivity shallow volume occurs in 2022, consistently with the fresh water discharge analysis (IHV, Fig. 13).
(ii) The smallest shallow high-resistivity volume is in 2024, with values similar to 2015, also aligning with the IHV.
(iii) In the deep region, the behaviour is opposite: the peak in high-resistivity volume is in 2024, with the lowest in 2022.

These deep variations are spatially evident in Figs 15(a)–(c), and in the plan-view reported in the bottom-left corner of each panel. The volume ratios of Figs 15(d) and (e) reinforce the previous statements, confirming that when shallow resistivity increases (now interpreted with the IHV as fresh water incomes), deep resistivity volumes decrease. Conversely, an increase in deep high-resistivity volumes is observed with a concurrent shallow resistivity decrease (reduced river discharge and freshwater), as seen in 2024.

The specular behaviour between the shallow and deep parts suggests a physical correlation, potentially indicating that shallow fresh water exchange influences the deeper, semiconfined aquifers. Interestingly, the analysis reveals the deep variations (<−50 m.a.s.l.) to concentrate beneath the river channel exchange area (see Fig. 15). As a preliminary interpretation, the deep changes may be induced by fresh water inflows from the Murray River on the floodplain. This shallow-deep communication is coherent with Yan *et al.* (2011), which report vertical connectivity in the aquifers and decreasing salinity with depth in the hydrostratigraphic column. As fresh water accumulates in the shallow floodplain, a downwards pressure gradient could be generated from the top of the hydrostratigraphic column, caused by the fresh volume sitting on more saline water and preventing its sinking. Thus, the peak fresh water volume in 2022 (Fig. 15d, shallow red anomaly) might have pushed saline water downward, resulting in the observed low-resistivity anomaly (Fig. 15d, deep blue anomaly). Conversely, in 2024, with reduced freshwater volumes, upward filtration could explain the increased deep resistivity anomaly (Fig. 15e) due to fresher deep water rising.

Although still preliminary, these deep variations align with the reported vertical interconnection of aquifers in the area, salinity trends and the localization of deep variations within the projection of the river channel. This suggests a potential relationship between shallow and deep hydrogeological domains, providing valuable insights for land managers and hydrogeological modelers. To expand and validate these interpretations, a new IHV should be planned as a future step, likely requiring more advanced hydrogeological modelling.

4 CONCLUSIONS

In this work, a novel simultaneous time-lapse inversion scheme is proposed and applied to a multitemporal AEM data set, proving able to handle differences in acquisition lines, flight heights and the use of different acquisition systems. Specifically, to address discrepancies in acquisition lines, the time-lapse scheme defines independently forward and model meshes, overcoming the modelling issue of non-coincident AEM soundings. Another modelling feature is the inclusion of AEM system flight height in the inversion parametrization, which proved important for achieving satisfactory data fitting and limiting artifact propagation in the models.

Along with this novel inversion approach, a new processing workflow for AEM monitoring data sets has been applied to effectively handle the multitemporal data, which posed new challenges compared to traditional ones, thus requiring dedicated treatment.

The field application focused on the Bookpurnong area, South Australia, along a floodplain sector of the Murray River, where multitemporal AEM surveys (2015, 2022 and 2024) were conducted to study the groundwater system and its evolution over time.

The time-lapse results showed small variations across most of the model—an important quality-control indicator considering that three different AEM system, with differences in flight paths and elevations, were incorporated into the modelling. This, combined with the presence of sharply bounded anomalies along the river channel, supported the effectiveness of the applied time-lapse scheme.

The time-lapse results were first assessed through misfit analysis, which showed an equal fit to the data compared to independent inversion while revealing significantly smaller variations in the models. The time-lapse model assessment was then expanded by comparing borehole resistivity log EM measurements on the floodplain, revealing an accurate match between the two.

The time-lapse shallow variations were ultimately validated and interpreted using an Independent Hydrogeological Validation approach, supporting the direct correlation between the hydrological stress of the Murray River and the hydrogeological response of the floodplain aquifers. In contrast, the deeper model variations showed an opposite response compared to the shallow ones, suggesting a possible correlation between shallow and deep aquifers.

We believe that the AEM time-lapse methodology developed in this work can be applied to monitor different types of processes, surpassing the capabilities of single-time AEM investigations and enabling accurate analysis of basin-scale processes.

ACKNOWLEDGMENTS

We acknowledge the Government of South Australia—Department of Environment and Water for providing the data. We thank CSIRO Mineral Resources for cofunding the research and for their support and hospitality during the research period. The study was co-funded also under the 'Progetto di Eccellenza 2023–2027: Le Georisorse per la Transizione Ecologica e lo Sviluppo Territoriale' by the Italian Ministry of University and Research. We extend our gratitude to Frans Schaars from Artesia Water Research Unlimited for the valuable discussions on the hydrogeological part of this work.

DATA AVAILABILITY

The data are available upon request to the authors and subject to final release under CSIRO and Government of South Australia agreement.

REFERENCES

Auken, E. *et al.*. 2015. An overview of a highly versatile forward and stable inverse algorithm for airborne, ground-based and borehole electromagnetic and electric data, *Explor. Geophys.,* **46,** 223–235.

Auken, E., Boesen, T. & Christiansen, A.V., 2017. A review of airborne electromagnetic methods with focus on geotechnical and hydrological applications from 2007 to 2017, in: *Advances in Geophysics,* 47–93, Elsevier.

Beamish, D. & Mattsson, A., 2003. Time-lapse airborne EM surveys across a municipal landfill, *JEEG,* **8,** 157–165.

Berens, V., Hatch, M., Wilson, T. & Hill, T., 2004. River-borne NanoTEM survey for location of salt accession to the River Murray at Loxton, *ASEG Extended Abstracts,* **2004,** 1–4.

Brown, C.M., 1989. Structural and stratigraphic framework of groundwater occurrence and surface discharge in the Murray Basin, southeastern Australia, *Journal of Australian Geology & Geophysics,* **11,** 127–146

Chandra, S. *et al.* 2021. Airborne electromagnetic signatures of an ancient river in the water-stressed Ganga Plain, Prayagraj, India: a potential groundwater repository, *Geophys. Res. Lett.,* **48,** e2021GL096100.

Chandra, S., Auken, E., Maurya, P.K., Ahmed, S. & Verma, S.K., 2019. Large scale mapping of fractures and groundwater pathways in crystalline hardrock by AEM, *Sci. Rep.,* **9,** 398.

Christensen, N.K., Ferre, T.P.A., Fiandaca, G. & Christensen, S., 2017. Voxel inversion of airborne electromagnetic data for improved groundwater model construction and prediction accuracy, *Hydrol. Earth Syst. Sci.,* **21,** 1321–1337.

Daily, W., Ramirez, A., LaBrecque, D. & Nitao, J., 1992. Electrical resistivity tomography of vadose water movement, *Water Resources Research,* **28,** 1429–1442

Dumont, M., Reninger, P.A., Aunay, B., Pryet, A., Jougnot, D., Join, J.L., Michon, L. & Martelet, G., 2021. Hydrogeophysical characterization in a volcanic context from local to regional scales combining airborne electromagnetism and magnetism, *Geophys. Res. Lett.,* **48,** e2020GL092000.

Engebretsen, K.W., Zhang, B., Fiandaca, G., Madsen, L.M., Auken, E. & Christiansen, A.V., 2022. Accelerated 2.5-D inversion of airborne transient electromagnetic data using reduced 3-D meshing, *Geophys. J. Int.,* **230,** 643–653.

Farquharson, C.G. & Oldenburg, D.W., 1998. Non-linear inversion using general measures of data misfit and model structure, *Geophys. J. Int.,* **134,** 213–227.

Fiandaca, G., Chen, J. & Zhang, B., 2024. EEMverter, a new modelling tool for electric and electromagnetic data with focus on induced polarization, in: *NSG 2024 30th European Meeting of Environmental and Engineering Geophysics. Presented at the NSG 2024 30th European Meeting of Environmental and Engineering Geophysics,* 1–5, European Association of Geoscientists & Engineers, Helsinki, Finland.

Fiandaca, G., Christiansen, A.V. & Auken, E., 2015b. Depth of investigation for multi-parameters inversions 2015, *NSG 2024 30th European Meeting of Environmental and Engineering Geophysics,* 1–5, European Association of Geoscientists & Engineers.

Fiandaca, G., Doetsch, J., Vignoli, G. & Auken, E., 2015. Generalized focusing of time-lapse changes with applications to direct current and time-domain induced polarization inversions, *Geophys. J. Int.,* **203,** 1101–1112.

Goebel, M., Knight, R. & Halkjær, M., 2019. Mapping saltwater intrusion with an airborne electromagnetic method in the offshore coastal environment, Monterey Bay, California, *J. Hydrol.: Reg. Stud.,* **23,** 100 602.

Hatch, M., Munday, T. & Heinson, G., 2010. A comparative study of in-river geophysical techniques to define variations in riverbed salt load and aid managing river salinization, *GEOPHYSICS,* **75,** WA135–WA147.

Hauser, J., Gunning, J., Munday, T. & Annetts, D., 2025. Time-lapse inversion of airborne electromagnetic data to recover the evolution of interfaces between freshwater and saltwater, *GEOPHYSICS,* **90,** 1–46.

Hayley, K., Pidlisecky, A. & Bentley, L.R., 2011. Simultaneous time-lapse electrical resistivity inversion, *J. Appl. Geophys.,* **75,** 401–411.

Karaoulis, M., Revil, A., Werkema, D.D., Minsley, B.J., Woodruff, W.F. & Kemna, A., 2011b. Time-lapse three-dimensional inversion of complex conductivity data using an active time constrained (ATC) approach: time-lapse complex conductivity imaging, *Geophys. J. Int.,* **187,** 237–251.

Karaoulis, M.C., Kim, J.-H. & Tsourlos, P.I., 2011a. 4D active time constrained resistivity inversion, *J. Appl. Geophys.,* **73,** 25–34.

Kim, J.-H., Yi, M.-J., Park, S.-G. & Kim, J.G., 2009. 4-D inversion of DC resistivity monitoring data acquired over a dynamically changing earth model, *J. Appl. Geophys.,* **68,** 522–532.

Knight, R., Smith, R., Asch, T., Abraham, J., Cannia, J., Viezzoli, A. & Fogg, G., 2018. Mapping aquifer systems with airborne electromagnetics in the Central Valley of California, *Groundwater,* **56,** 893–908.

LaBrecque, D.G. & Yang, X., 2001. Difference Inversion of ERT Data: a Fast Inversion Method for 3-D In Situ Monitoring, *Journal of Environmental and Engineering Geophysics,* **6,** 83–89

Miller, C.R., Routh, P.S., Brosten, T.R., & McNamara, J.P., 2008. Application of time-lapse ERT imaging to watershed characterization, *GEOPHYSICS,* **73** G7–G17

Minsley, B.J., Rigby, J.R., James, S.R., Burton, B.L., Knierim, K.J., Pace, M.D.M., Bedrosian, P.A. & Kress, W.H., 2021. Airborne geophysical surveys of the lower Mississippi Valley demonstrate system-scale mapping of subsurface architecture, *Commun. Earth Environ*., **2,** 131.

Munday, T. & Soerensen, C., 2018. Resolving changes to freshwater lens systems in a "sea of Salinity" using Multi-date Airborne EM, *ASEG Extended Abstracts,* **2018,** 1–8.

Munday, T.J., Hill, A.J., Wilson, T., Hopkins, B., Telfer, A.L., White, G.J. & Green, A., 2005. Combining geology and geophysics to develop a hydrogeologic framework for salt interception in the Loxton Sands aquifer, central Murray Basin Australia, *Australas. J. Water Resour.,* **9,** 163–168.

Oldenborger, G.A., Knoll, M.D., Routh, P.S. & LaBrecque, D.G., 2007. Time-lapse ERT monitoring of an injection/withdrawal experiment in a shallow unconfined aquifer, *GEOPHYSICS,* **72,** F177–F187.

SA Water, 2018. River Murray Flow Data

Signora, A., 2025a. Time lapse Airborne EM for monitoring the evolution of a saltwater aquifer—the Bookpurnong case study (video a),

Signora, A., 2025c. Time lapse Airborne EM for monitoring the evolution of a saltwater aquifer—the Bookpurnong case study (video c),

Sorensen, K.I. & Auken, E., 2004. SkyTEM–a new high-resolution helicopter transient electromagnetic system, *Explor. Geophys.,* **35,** 194–202.

Sullivan, N.A.L., Viezzoli, A. & Fiandaca, G., 2024. EEMstudio: process and model electric and electromagnetic data with a QGIS plugin 2024, *NSG 2024 30th European Meeting of Environmental and Engineering Geophysics,* pp. 1–5, European Association of Geoscientists & Engineers.

Van Engelen, J., Oude Essink, G.H.P., Kooi, H. & Bierkens, M.F.P., 2018. On the origins of hypersaline groundwater in the Nile Delta aquifer, *J. Hydrol.,* **560,** 301–317.

Viezzoli, A., Auken, E. & Munday, T., 2009. Spatially constrained inversion for quasi 3D modelling of airborne electromagnetic data—an application for environmental assessment in the Lower Murray Region of South Australia, *Explor. Geophys.,* **40,** 173–183.

Viezzoli, A., Jørgensen, F. & Sørensen, C., 2013. Flawed processing of airborne EM data affecting hydrogeological interpretation, *Groundwater,* **51,** 191–202.

Viezzoli, A., Munday, T., Auken, E., Christiansen, A.V. & Wilson, G.A., 2010. Accurate quasi 3D versus practical full 3D inversion of AEM data—the Bookpurnong case study, **2010,** 23–31.

Xiao, L., Fiandaca, G., Zhang, B., Auken, E. & Christiansen, A.V., 2022b. Fast 2.5D and 3D inversion of transient electromagnetic surveys using the octree-based finite-element method, *GEOPHYSICS,* **a87,** E267–E277.

Yan, W., Howles, S., Howe, B. & Hill, T., 2005. Loxton—Bookpurnong numerical Groundwater Model 2005, South Australia. Department of Water, Land and Biodiversity Conservation. DWLBC Report 2005/17, AWI 2005

Yan, W., Li, C. & Woods, J., 2011. *Loxton-Bookpurnong Numerical Groundwater Model 2011,* Government of South Australia, DFW Technical Report 2011/22, AWI 2011

Zhang, B., Engebretsen, K.W., Fiandaca, G., Cai, H. & Auken, E., 2021. 3D inversion of time-domain electromagnetic data using finite elements and a triple mesh formulation, *GEOPHYSICS,* **86,** E257–E267.

APPENDIX A

In the following we present a test to assess the sensitivity in the deepest portion of the time-lapse models to evaluate the reliability of the resistivity anomalies/variations observed at these depths. Specifically, the test involved the computation of forward responses using models in which the deep variations have been removed. In particular, the deepest portions of the 2022 and 2024 models—(below 80 m, see Fig. 11)—have been modified, swapping the 2015 model into the 2022 one and the 2022 into the 2024 model. The forward responses resulted in increased data misfit for the 2022 and 2024 modified models, as reported in Table A1.

To spatially localize this increase, Fig. A1 presents a 3-D view of the misfit, similar to what is shown in Fig. 9. Specifically, panels (a) and (b) show the misfit distribution of the time-lapse models already presented in the manuscript (Figs 9d and g), but this time from a bottom-up view. Figs A1(c) and (d) display the misfit of the forward modelling test with swapped bottom part in the starting models, showing how the increase is almost entirely localized where the deep resistivity anomalies develop.

To further support this analysis, panels (e)–(h), display the ratio between the 'swapped' and original misfit, highlighting again how the increased misfit is confined in correspondence with the deep structure of interest. From the top view (panels g and h), no appreciable misfit differences are visible, as expected since the models in that region were identical.

These results confirm that without the presence of these deep structures in the time-lapse model it is not possible to fit the data as well, supporting their data-driven rather than model-driven origin.

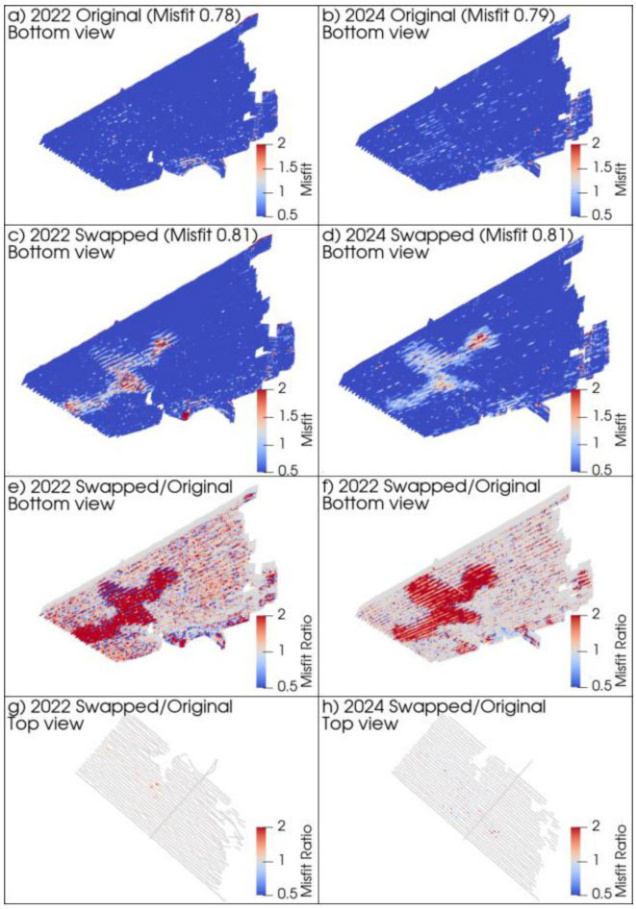

Figure A1. (a, b) Gate-by-gate 3-D distribution of the misfit for the 2022 and 2024 time-lapse models presented in the manuscript. (c, d) Same distribution for the forward modelling test in which the deep parts of the 2022 and 2024 models have been changed. (e, f) Ratio between original and swapped misfit for the same years, shown from a bottom view. (g, h) Same ratio, visualized from a top view.

Table A1. Misfit of the time-lapse models presented in the manuscript (first row) for the 2015, 2022 and 2024 models, and misfit of the forward test where the deep portions of the 2022 and 2024 models have been changed (second row)

	2015	2022	2024
Original model misfits	1.22	0.78	0.79
Swapped model misfits	1.22	0.81	0.81